

Cold Dust and Low [O III]/[C II] Ratios: an Evolved Star-forming Population at Redshift 7

Hiddo S. B. Algera,^{1,2*} Hanae Inami,¹ Laura Sommovigo,³ Yoshinobu Fudamoto,^{4,2} Raffaella Schneider,^{5,6} Luca Graziani,^{5,6} Pratika Dayal,⁷ Rychard Bouwens,⁸ Manuel Aravena,⁹ Elisabete da Cunha,^{10,11} Andrea Ferrara,³ Alexander P. S. Hygate,⁸ Ivana van Leeuwen,⁸ Ilse De Looze,^{12,13} Marco Palla,^{12,14} Andrea Pallottini,³ Renske Smit,¹⁵ Mauro Stefanon,^{16,17} Michael Topping,¹⁸ and Paul P. van der Werf⁸

¹Hiroshima Astrophysical Science Center, Hiroshima University, 1-3-1 Kagamiyama, Higashi-Hiroshima, Hiroshima 739-8526, Japan

²National Astronomical Observatory of Japan, 2-21-1, Osawa, Mitaka, Tokyo, Japan

³Scuola Normale Superiore, Piazza dei Cavalieri 7, I-56126 Pisa, Italy

⁴Waseda Research Institute for Science and Engineering, Faculty of Science and Engineering, Waseda University, 3-4-1 Okubo, Shinjuku, Tokyo 169-8555, Japan

⁵Dipartimento di Fisica, Sapienza, Università di Roma, Piazzale Aldo Moro 5, I-00185 Roma, Italy

⁶INAF/Osservatorio Astronomico di Roma, via Frascati 33, I-00078 Monte Porzio Catone, Roma, Italy

⁷Kapteyn Astronomical Institute, University of Groningen, P.O. Box 800, 9700 AV Groningen, The Netherlands

⁸Leiden Observatory, Leiden University, NL-2300 RA Leiden, Netherlands

⁹Instituto de Estudios Astrofísicos, Facultad de Ingeniería y Ciencias, Universidad Diego Portales, Av. Ejército 441, Santiago, Chile

¹⁰International Centre for Radio Astronomy Research, University of Western Australia, 35 Stirling Hwy, Crawley, 26WA 6009, Australia

¹¹ARC Centre of Excellence for All Sky Astrophysics in 3 Dimensions (ASTRO 3D)

¹²Sterrenkundig Observatorium, Ghent University, Krijgslaan 281 - S9, 9000 Gent, Belgium

¹³Dept. of Physics & Astronomy, University College London, Gower Street, London WC1E 6BT, United Kingdom

¹⁴INAF - OAS, Osservatorio di Astrofisica e Scienza dello Spazio di Bologna, via Gobetti 93/3, 40129 Bologna, Italy

¹⁵Astrophysics Research Institute, Liverpool John Moores University, 146 Brownlow Hill, Liverpool L3 5RF, UK

¹⁶Departament d'Astronomia i Astrofísica, Universitat de València, C. Dr. Moliner 50, E-46100 Burjassot, València, Spain

¹⁷Unidad Asociada CSIC "Grupo de Astrofísica Extragaláctica y Cosmología" (Instituto de Física de Cantabria - Universitat de València)

¹⁸Steward Observatory, University of Arizona, 933 N Cherry Ave, Tucson, AZ 85721, USA

Accepted XXX. Received YYY; in original form ZZZ

ABSTRACT

We present new ALMA Band 8 (rest-frame 90 μm) continuum observations of three massive ($M_{\star} \approx 10^{10} M_{\odot}$) galaxies at $z \approx 7$ previously detected in [C II]158 μm and underlying dust continuum emission in the Reionization Era Bright Emission Line Survey (REBELS). We detect dust emission from two of our targets in Band 8 (REBELS-25 and REBELS-38), while REBELS-12 remains undetected. Through optically thin modified blackbody fitting, we determine dust temperatures of $T_{\text{dust}} \approx 30 - 35$ K in both of the dual-band detected targets, indicating they are colder than most known galaxies at $z \sim 7$. Moreover, their inferred dust masses are large ($M_{\text{dust}} \approx 10^8 M_{\odot}$), albeit still consistent with models of high-redshift dust production. We furthermore target and detect [O III]88 μm emission in both REBELS-12 and REBELS-25, and find $L_{[\text{O III}]} / L_{[\text{C II}]} \approx 1 - 1.5$ – low compared to the $L_{[\text{O III}]} / L_{[\text{C II}]} \geq 2 - 10$ observed in the known $z \geq 6$ population thus far. We argue the lower line ratios are due to a comparatively weaker ionizing radiation field resulting from the less starburst nature of our targets, although the possibility of REBELS-12 being a merger of an [O III]-bright and [O III]-faint component prevents the unambiguous interpretation of its [O III]/[C II] ratio. Nevertheless, a low burstiness forms a natural explanation for the cold dust temperatures and low [O III] $\lambda\lambda$ 4959, 5007 + H β equivalent widths of REBELS-25 and REBELS-38. Overall, these observations provide evidence for the existence of a massive, dust-rich galaxy population at $z \approx 7$ which has previously experienced vigorous star formation, but is currently forming stars in a steady, as opposed to bursty, manner.

Key words: galaxies: evolution – galaxies: high-redshift – submillimeter: galaxies

1 INTRODUCTION

Understanding how the evolution of galaxies proceeds across cosmic time is one of the fundamental goals of modern day astronomy.

Over the last two decades, ever-increasing samples of high-redshift ($z \geq 6$) galaxies are being discovered, largely based on observations probing their rest-frame ultraviolet (UV) and optical emission (e.g., McLure et al. 2013; Bouwens et al. 2015; Finkelstein et al. 2015; Stark 2016; Oesch et al. 2018; Stefanon et al. 2019). More recently, with the launch of the *James Webb Space Telescope* (JWST), an even

* E-mail: algera@hiroshima-u.ac.jp

clearer window on the rest-frame UV to near-infrared (NIR) emission of high-redshift galaxies has been opened (e.g., [Atek et al. 2022](#); [Castellano et al. 2022](#); [Harikane et al. 2022](#); [Naidu et al. 2022](#); [Yan et al. 2022](#)). However, observations of galaxies across all redshifts have long demonstrated that the presence of dust severely impacts their detectability at short wavelengths, as well as the information that can be extracted from their UV-to-NIR spectral energy distributions (SEDs; e.g., [Draine 1989, 2003](#); [Calzetti et al. 2000](#); [Blain et al. 2002](#); [Casey et al. 2014](#); [Dudzevičiūtė et al. 2020](#)). Specifically, light emitted at UV and optical wavelengths is readily absorbed by dust, and subsequently re-emitted at longer wavelengths. As a result, UV and optical observations alone provide only an incomplete and biased view of the high redshift galaxy population, necessitating the use of observations at far-infrared wavelengths and beyond.

In the last several years, the Atacama Large Millimeter/submillimeter Array (ALMA) has enabled the detailed study of the dust and interstellar medium (ISM) properties of distant galaxies at (sub-)millimeter wavelengths (see [Hodge & da Cunha 2020](#) for a review). Various emission lines, most significantly the [C II]158 μm and [O III]88 μm lines, are now routinely used to probe the ISM conditions of high-redshift sources and to constrain their systemic redshifts ([Hashimoto et al. 2018, 2019](#); [Carniani et al. 2020](#); [Harikane et al. 2020](#); [Bouwens et al. 2022](#); [Schouws et al. 2022a](#); [Witstok et al. 2022](#)). Given its high ionization potential, [O III] emission predominantly emanates from dense HII regions close to sites of star formation ([Cormier et al. 2012](#); [Vallini et al. 2017](#); [Arata et al. 2020](#)). [C II], on the other hand, has a variety of origins, but is thought to mostly originate in photo-dissociation regions (PDRs; [Stacey et al. 2010](#); [Vallini et al. 2015](#); [Gullberg et al. 2015](#); [Lagache et al. 2018](#); [Cormier et al. 2019](#)). While in nearby starburst galaxies the [C II] line is the dominant coolant of the ISM (i.e., $L_{[\text{O III}]} / L_{[\text{C II}]} < 1$; [De Looze et al. 2014](#); [Díaz-Santos et al. 2017](#)), at high redshift [O III] is observed to become more luminous ([Carniani et al. 2020](#); [Harikane et al. 2020](#); [Witstok et al. 2022](#)). This has been attributed to a highly ionized ISM resulting from strong starburst activity ([Inoue et al. 2016](#); [Ferrara et al. 2019](#); [Arata et al. 2020](#); [Vallini et al. 2021](#); [Sugahara et al. 2022](#)), possibly in combination with other effects such as a low metallicity and/or a low carbon abundance resulting from a top-heavy initial mass function (IMF; e.g., [Arata et al. 2020](#); [Lupi & Bovino 2020](#); [Katz et al. 2022](#)).

Albeit generally harder to detect at high redshift than the [O III] and [C II] lines, the underlying dust continuum emission is also occasionally observed in $z \gtrsim 6.5$ galaxies (e.g., [Watson et al. 2015](#); [Laporte et al. 2017, 2019](#); [Bowler et al. 2018](#); [Schouws et al. 2022b](#); [Witstok et al. 2022](#); see also [Inami et al. 2022](#) for a recent compilation). The Reionization Era Bright Emission Line Survey (REBELS; [Bouwens et al. 2022](#)) in particular has provided the first statistical insights into the dust and ISM properties of UV-selected galaxies at $z \gtrsim 6.5$. [Inami et al. \(2022\)](#) show that dust is common in these high-redshift sources even for UV-selected galaxies, detecting it in $\geq 40\%$ of REBELS targets. Additionally, [Algera et al. \(2023\)](#) find that, even at $z = 7$, dust-obscured star formation still accounts for $\sim 30\%$ of the overall cosmic star formation rate density (see also [Barrufet et al. 2023](#)).

Not only may dust conceal an appreciable fraction of star formation at high redshift, it is also thought to be important for studies of reionization, as dust is capable of attenuating ionizing photons (e.g., [Hayes et al. 2011](#); [Katz et al. 2017](#); [Glatzle et al. 2019](#)). Furthermore, dust alters the chemical equilibrium in galaxies and can provide an important pathway for the formation of molecular hydrogen, thereby providing the fuel for subsequent star formation ([Gould & Salpeter 1963](#); [Hirashita & Ferrara 2002](#)).

Despite the importance of dust in the early Universe, the pathways through which significant dust reservoirs can already be assembled in only a fraction of a gigayear remain actively studied (e.g., [Todini & Ferrara 2001](#); [Mancini et al. 2015](#); [Michałowski 2015](#); [Popping et al. 2017](#); [Behrens et al. 2018](#); [Vijayan et al. 2019](#); [Graziani et al. 2020](#); [Sommovigo et al. 2020](#); [Dayal et al. 2022](#); [Di Cesare et al. 2023](#)). However, to date, the bulk of the dust detections at $z \gtrsim 7$ are limited to a single continuum measurement, such that dust masses and infrared luminosities often need to be extrapolated from a single wavelength (e.g., [Bowler et al. 2018](#); [Schouws et al. 2022b](#); [Inami et al. 2022](#)). While inventive models have been developed to predict dust parameters (temperature, mass) from single-band continuum data (e.g., [Inoue et al. 2020](#); [Sommovigo et al. 2021](#); [Fudamoto et al. 2022a](#)), such methods remain to be tested on larger samples of distant galaxies to fully establish their robustness and predictive power.

Accurately measuring dust properties observationally, however, requires multi-band continuum photometry. One of the key parameters that can be constrained when at least two ALMA bands are available, is the dust temperature T_{dust} ([Hodge & da Cunha 2020](#); [Bakx et al. 2021](#)). Given that the infrared luminosity, and therefore the obscured star formation rate (SFR; e.g., [Kennicutt & Evans 2012](#)), scales as $L_{\text{IR}} \propto M_{\text{dust}} T_{\text{dust}}^{\beta+4}$ with $\beta \sim 1.5 - 2$, small variations in dust temperature imply potentially large variations in dust mass or infrared luminosity. As such, accurately measuring dust temperatures is crucial for a robust census of dust-obscured cosmic star formation and for properly constraining early dust enrichment.

Several observations ([Schreiber et al. 2018](#); [Laporte et al. 2019](#); [Bakx et al. 2020](#); [Viero et al. 2022](#)) and simulations ([Behrens et al. 2018](#); [Ma et al. 2018](#); [Liang et al. 2019](#); [Pallottini et al. 2022](#); [Vijayan et al. 2022](#)) have suggested that dust may be hotter at high redshift. Given that observationally dust mass and temperature are often degenerate, warmer dust lowers the need for massive dust reservoirs. From a physical perspective, hot dust may be expected in high-redshift galaxies, due to their generally compact sizes ([Van der Wel et al. 2014](#); [Fudamoto et al. 2022b](#)) and correspondingly high star formation rate surface densities (e.g., [Schreiber et al. 2018](#)). In addition, when total dust masses are modest, the available energy injected by stars per unit dust mass increases, thereby increasing the overall heating ([Sommovigo et al. 2022b](#)). However, given that multi-band ALMA observations of galaxies in the epoch of reionization remain rare, are often limited to non-detections or low-S/N measurements, and are potentially biased to warmer and therefore more luminous sources, larger samples of high-redshift galaxies with robust observational constraints on their dust temperatures are essential.

In this paper, we investigate the dust properties of three $z \approx 7$ galaxies from the REBELS survey using combined ALMA Band 6 and Band 8 observations. In Section 2 we introduce the REBELS survey and the newly acquired Band 8 observations, followed by the identification of dust continuum and [O III]88 μm emission in our targets in Section 3. Section 4 details our method of fitting far-infrared SEDs, while in Section 5 we describe our results. In Section 6 we discuss our findings in detail, and finally we summarize them in Section 7. Throughout this work, we assume a standard Λ CDM cosmology, with $H_0 = 70 \text{ km s}^{-1} \text{ Mpc}^{-1}$, $\Omega_m = 0.30$ and $\Omega_\Lambda = 0.70$. We further adopt a [Chabrier \(2003\)](#) IMF across a mass range of $0.1 - 300 M_\odot$.

2 DATA

2.1 REBELS

REBELS is a Cycle 7 ALMA Large Program targeting 40 UV-bright galaxies with robustly measured photometric redshifts in the range $6.5 \lesssim z_{\text{phot}} \lesssim 9.5$. Galaxies were targeted either in the [C II] 158 μm (36 sources) or [O III] 88 μm (4 sources) emission line through a spectral scanning technique, designed to cover $\sim 90\%$ of the photometric redshift probability distribution. In tandem, sensitive observations of the dust continuum are therefore obtained. The observing strategy as well as a summary of initial results of the REBELS program are outlined in detail in Bouwens et al. (2022). In the observations taken during Cycle 7, 23 galaxies were detected in [C II] emission, and 16 were detected in dust emission at rest-frame 158 μm . For a full analysis of the [C II]-detected sources, we refer the reader to Schouws et al. (in prep), while the dust continuum detections are presented in Inami et al. (2022).

The UV luminosities of the full REBELS sample have been measured by Stefanon et al. (in prep), while stellar masses are presented in Topping et al. (2022). The latter study makes use of SED-fitting code Prospector (Johnson et al. 2021) under the assumption of a non-parametric star formation history (SFH). Such SFHs are particularly well-suited to model any older stellar populations that may be present, even if outshone by more recent bursts of star formation (e.g., Leja et al. 2019, 2020; Topping et al. 2022; Whitler et al. 2022). The REBELS sample spans a stellar mass range of $\log_{10}(M_{\star}/M_{\odot}) = 8.8 - 10.4$; in this work, we focus on three select galaxies at the massive end.

2.1.1 Our Targets

This work presents new ALMA observations of three $z \approx 7$ galaxies drawn from the REBELS survey: REBELS-12, REBELS-25 and REBELS-38. All three sources have accurate spectroscopic redshifts determined from their bright [C II] emission lines and are robustly detected in underlying rest-frame $\sim 160 \mu\text{m}$ dust continuum emission.

REBELS-25 and REBELS-38 are the two brightest galaxies among REBELS, both in terms of [C II] luminosity and Band 6 dust continuum flux density. REBELS-25, in particular, has previously been classified as the only Ultra-luminous Infrared Galaxy (ULIRG; defined as having $L_{\text{IR}} > 10^{12} L_{\odot}$) at $z > 7$ (Hygate et al. 2022), based on the high infrared luminosity predicted from its single-band dust continuum detection (Inami et al. 2022; Sommovigo et al. 2022a). REBELS-12, the fourth most luminous [C II]-emitter in REBELS, is particularly interesting as it is neighbored by a coeval, optically dark galaxy (Fudamoto et al. 2021). As such, it could potentially be part of a larger cosmic structure in the early Universe.

All three of our targets are particularly massive ($M_{\star} \gtrsim 10^{10} M_{\odot}$; Topping et al. 2022), making them prime candidates for hosting massive dust reservoirs in the early Universe (e.g., Di Cesare et al. 2023). Current multi-band ALMA studies of high-redshift dust have focused predominantly on lower-mass galaxies, including intrinsically faint ones aided by gravitational lensing (e.g., Hashimoto et al. 2019; Tamura et al. 2019; Akins et al. 2022). Through targeting REBELS galaxies, we complement these earlier studies by investigating the dust properties at high redshift across a wider range of galaxy types.

Table 1. Summary of the ALMA Band 8 continuum image properties of our three REBELS targets.

ID	ν_{cen}	$t_{\text{int}}^{\text{a}}$	RMS	$\theta_{\text{major}}^{\text{b}}$	$\theta_{\text{minor}}^{\text{b}}$	PA ^b
	[GHz]	min	[$\mu\text{Jy bm}^{-1}$]	[asec]	[asec]	[deg]
REBELS-12	401.4	83.2	48.9	0.61	0.45	58.5
REBELS-25	403.4	12.6	111.7	1.09	0.64	-63.4
REBELS-38	405.0	38.3	41.9	0.61	0.48	56.9

^aIntegration time (on source) in minutes

^bSize and orientation of the synthesized beam

2.2 ALMA Band 8 Observations

The new Band 8 observations ($\lambda_{\text{obs}} \approx 750 \mu\text{m}$), obtained in ALMA Cycle 8, are drawn from ALMA programs 2021.1.00318.S (REBELS-25, REBELS-38; PI: Inami) and 2021.1.01297.S (REBELS-12; PI: Fudamoto). REBELS-25 and REBELS-38 are in the phase center of their respective Band 8 observations, while the primary beam sensitivity of the Band 8 map at the location of REBELS-12 is $\approx 70\%$ of the peak. This is due to the simultaneous observation of its serendipitously detected optically dark neighbor, roughly 11.5 arcsec from the main target (Fudamoto et al. 2021). The observations of this neighbor will be presented in Fudamoto et al. (in prep), while this paper focuses solely on the main REBELS targets.

The Band 8 data were calibrated using the ALMA pipeline incorporated in CASA (version 6.2.1). Continuum imaging was performed using CLEAN with natural weighting to optimize sensitivity, excluding channels contaminated by the [O III] emission line (see below). Details of the final images, including the on-source time, RMS noise, central frequency and resolution, are listed in Table 1.

For REBELS-12 and REBELS-25, the spectral setup also covers the [O III] emission line. The line was not targeted in REBELS-38 due to its lower redshift, placing [O III] in a window of low atmospheric transmission. We create datacubes of both REBELS-12 and REBELS-25 in order to identify possible [O III] emission. For this, we first run CASA task UVCONTSUB to subtract any continuum emission, assuming a zeroth-order polynomial. We use natural weighting to produce the cubes, and create initial moment zero maps by collapsing the channels where the emission line is expected based on the known [C II] redshift and full width at half maximum (FWHM). We fit the line center and FWHM iteratively until the fit converges to a stable solution, and then create a moment-0 map by collapsing channels across the FWHM to maximize its S/N. In the continuum imaging of REBELS-12 and REBELS-25, we ensured that the spectral range contaminated by the [O III] emission line was excluded by removing all channels within $3\times$ the [O III] FWHM around the line center.

3 IDENTIFICATION OF CONTINUUM AND [O III] EMISSION

To identify continuum emission in the ALMA Band 8 images, we use PyBDSF (Mohan & Rafferty 2015), following the source detection procedure in the original REBELS survey (Inami et al. 2022). PyBDSF finds islands of contiguous emission and fits these with two-dimensional Gaussians to extract their flux densities. We detect Band 8 continuum emission in REBELS-25 at a peak S/N of 4.4σ , while the continuum remains undetected in REBELS-12 ($< 3\sigma$). The new Band 8 observations of REBELS-38 highlight a two-component

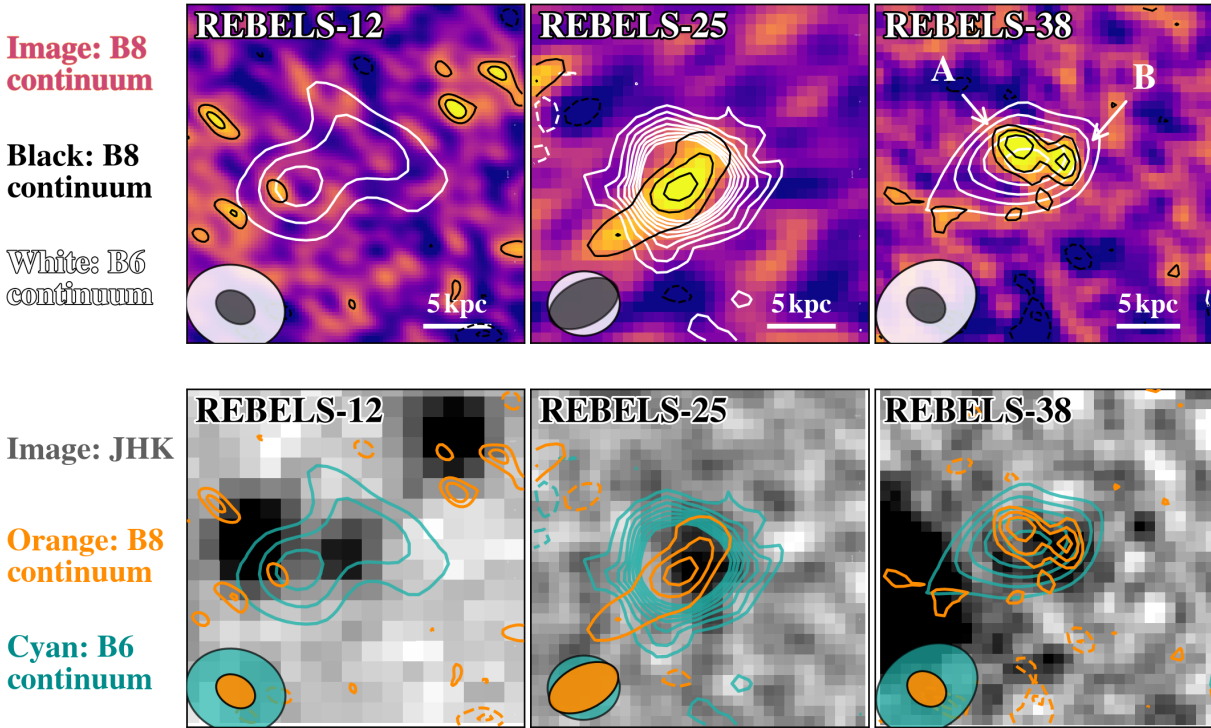


Figure 1. The three sources analyzed in this work – from left to right, REBELS-12, REBELS-25 and REBELS-38. All cutouts span an area of $5'' \times 5''$. The **top row** shows the Band 8 continuum maps at their native resolution in the background, with black contours outlining the continuum emission at the 2, 3 and 4σ levels where σ is the local RMS in the image. REBELS-12 is undetected in the Band 8 continuum data, while REBELS-25 and REBELS-38 are detected at a peak S/N in the untapered maps of 4.4 and 4.3σ , respectively. The overlaid white contours show the Band 6 continuum emission from 2 – 10σ in steps of 1σ . The black (white) beam in the corner represents the FWHM of the Band 8 (Band 6) observations. The **bottom row** shows the same Band 6 (cyan) and Band 8 (orange) contours on top of stacked ground-based JHK-imaging. In the higher resolution Band 8 observations, REBELS-38 appears to separate into two dusty components, labeled A and B in the top right image.

dust morphology that was not visible in the original Band 6 data. The two dust peaks are individually detected at a S/N of 4.3σ and 4.1σ . This interesting morphology of REBELS-38 is discussed further in Section 5.1.3.

We show the Band 8 continuum images of our targets in the top row of Figure 1, with the Band 6 continuum contours overlaid. In addition, in the bottom row, we show the Band 8 continuum contours on top of stacked ground-based JHK images. For REBELS-12, the ground-based imaging is from the VIDEO survey (Jarvis et al. 2013), while for REBELS-25 and REBELS-38 the images are from COSMOS/UltraVISTA DR4 (Scoville et al. 2007; McCracken et al. 2012). The rest-frame optical images for REBELS-12 were aligned to the Gaia DR3 catalog by Inami et al. (2022), while the UltraVISTA JHK images were already aligned to Gaia DR1 as part of the fourth data release, ensuring an astrometric accuracy of $0''.03 - 0''.12$.

We additionally create tapered maps (using the UVTAPER parameter in TCLEAN) of REBELS-25 and REBELS-38 in order to match the Band 6 resolution and more fairly compare the continuum flux densities across wavelength. The Band 6 continuum images of REBELS-25 and REBELS-38, created using natural weighting, have a resolution of $1''.1 \times 0''.94$ and $1''.6 \times 1''.2$, respectively (Inami et al. 2022). The Band 8 image of REBELS-25 has an asymmetric native beam (Table 1), and we therefore taper the beam to a circular Gaussian of $1''.1$. For REBELS-38, we apply tapering to obtain a circular beam

of $1''.2$ in order to better match the Band 6 resolution. This tapered beam is sufficiently coarse that the two dust peaks are blended together, while ensuring the continuum sensitivity remains adequate.

We re-run PyBDSF to extract the continuum flux densities from these tapered maps, and compile these – as well as the untapered flux densities and other relevant physical properties of our targets – in Table 2. The significance of the continuum detection in the tapered map of REBELS-25 is comparable to that at the native resolution. For REBELS-38, on the other hand, the two dust components are blended together in the tapered image, such that the detection significance of the peak flux density is enhanced to 5.3σ . The flux in the tapered map is consistent with the sum of the two individual components as measured in the higher resolution image. In what follows, we utilize the continuum flux densities obtained from the tapered images for both REBELS-25 and REBELS-38, unless specified otherwise.

For REBELS-12 and REBELS-25, the spectral setup also covers the [O III] emission line. We show the corresponding moment-0 maps in Figure 2, comparing to the spatial distribution of the dust continuum emission (top row) and rest-frame UV emission (bottom). We detect the [O III] line in both REBELS-12 and REBELS-25, at a significance of 5.6σ and 5.1σ , respectively, measured as the peak S/N in the moment-0 map. To extract the 1D spectra, we sum all pixels in the moment-0 map with significance $\geq 2\sigma$ within a radius

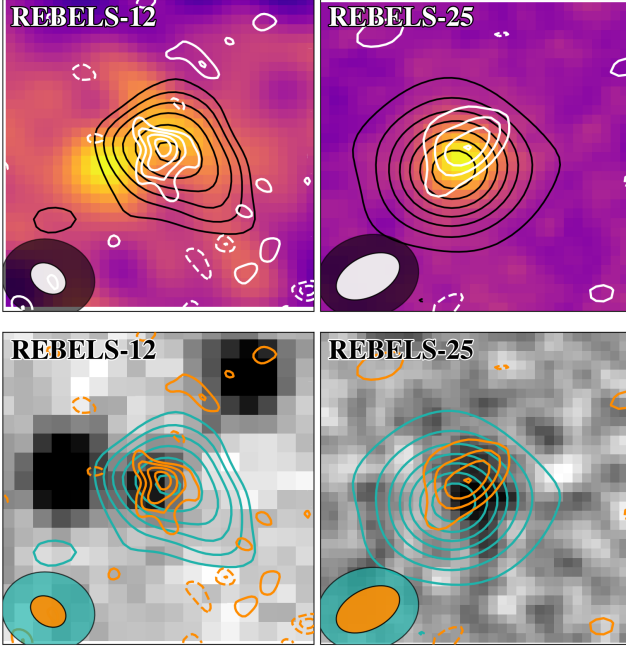


Figure 2. Top: Moment-0 maps of the [O III] emission in REBELS-12 and REBELS-25 (white contours), on top of [C II] emission (black contours) and Band 6 dust continuum emission (background; $5'' \times 5''$). **Bottom:** The moment-0 maps on top of stacked JHK images. Here, [O III] and [C II] are shown in orange and cyan, respectively, for visual clarity. In all panels, [O III] contours range from $2 - 5\sigma$, and the [C II] contours start at 3σ and increase in steps of 1σ (steps of 4σ) for REBELS-12 (REBELS-25). The beam sizes corresponding to the emission line data are shown in the bottom left corner. In REBELS-25, the [C II], [O III] and rest-frame $158 \mu\text{m}$ dust emission are roughly co-spatial, while the peak of the dust continuum in REBELS-12 appears offset from the emission lines.

of $2''.0$ around the peak pixel. We discuss the 1D spectra, as well as the morphology of our targets, in further detail in Section 5.2.

4 DUST SED FITTING

4.1 Modified Blackbody Formalism

When multi-frequency observations of a galaxy’s dust continuum emission are available, it is possible to fit a physical model to the dust emission to constrain its properties (e.g., dust mass and temperature, infrared luminosity). Generally, a modified blackbody (MBB) is used (e.g., Greve et al. 2012; Liang et al. 2019; Jones et al. 2020), which depends on three main fitting parameters: the dust temperature (T_{dust}), the dust mass (M_{dust}) and the dust emissivity index (β). In addition, the dust may be optically thick at short wavelengths ($\lambda \lesssim 100 - 200 \mu\text{m}$; e.g., Casey 2012), introducing an additional parameter $\lambda_{\text{thick}} = c/\nu_{\text{thick}}$ where the optical depth equals unity. The most general functional form of an optically thick modified blackbody may therefore be written as

$$S_{\nu_{\text{obs}}} = \left(\frac{1+z}{d_L^2} \right) \left(\frac{1 - e^{-\tau_\nu}}{\tau_\nu} \right) M_{\text{dust}} \kappa_\nu B_\nu(T_{\text{dust}}). \quad (1)$$

Here ν and ν_{obs} represent frequencies in the source rest- and ob-

served frame, respectively,¹ d_L is the luminosity distance at redshift z and $\kappa_\nu = \kappa_0(\nu/\nu_0)^\beta$ is the dust mass absorption coefficient at normalization frequency ν_0 . We adopt Milky Way dust with $\kappa_0 = \kappa(\nu_0 = 1900 \text{ GHz}) = 10.41 \text{ cm}^2 \text{ g}^{-1}$, which appears best suited to match the dust in high-redshift sources (see e.g., Behrens et al. 2018; Schouws et al. 2022b; Ferrara et al. 2022) and has been used throughout the series of REBELS papers to model dust properties (e.g., Inami et al. 2022; Sommovigo et al. 2022a). The optical depth is defined as the integral over the line of sight via $\tau_\nu = \int \alpha_\nu ds = \int \kappa_\nu \rho_{\text{dust}} ds$, where α_ν is the absorption coefficient and ρ_{dust} is the dust mass density. As such, the optical depth can be written as $\tau_\nu = \kappa_\nu \Sigma_{\text{dust}}$, where Σ_{dust} is the dust mass surface density. Equivalently, we may write $\tau_\nu = (\nu/\nu_{\text{thick}})^\beta = (\lambda/\lambda_{\text{thick}})^{-\beta}$. In the limit where the dust is optically thin across all frequencies, that is $\tau_\nu \ll 1$, the term $(1 - e^{-\tau_\nu})/\tau_\nu \approx 1$ and we recover the general functional form of an optically thin MBB.

We must further consider that at $z \sim 7$ the cosmic microwave background (CMB) is sufficiently warm [$T_{\text{CMB}}(z=7) = T_{\text{CMB},0} \times (1+z) = 21.8 \text{ K}$] that it may contribute to the heating of the dust. As shown by Da Cunha et al. (2013), the “effective” dust temperature of a high-redshift galaxy, $T_{\text{dust},z}$, is related to the dust temperature it would have at $z=0$ via

$$T_{\text{dust},z} = \left(T_{\text{dust},0}^{4+\beta} + T_{\text{CMB},0}^{4+\beta} \left[(1+z)^{4+\beta} - 1 \right] \right)^{1/(4+\beta)}. \quad (2)$$

However, not only is the CMB causing dust to be warmer at high redshift, it also acts as a background against which the submillimeter emission from a galaxy is observed, since interferometers are insensitive to large-scale uniform emission (Da Cunha et al. 2013). The magnitude of this effect depends on the observed (i.e., CMB-heated) temperature of the dust and the temperature of the CMB itself, and is demonstrated by Da Cunha et al. (2013) to be

$$\frac{S_\nu^{\text{no contrast}}}{S_\nu^{\text{against CMB}}} = \left(1 - \frac{B_\nu(T_{\text{CMB},z})}{B_\nu(T_{\text{dust},z})} \right)^{-1}. \quad (3)$$

Combining the above equation with Equation 1, we may write the general functional form of a modified blackbody affected by the CMB as

$$S_\nu = \left(\frac{1+z}{d_L^2} \right) \left(\frac{1 - e^{-\tau_\nu}}{\tau_\nu} \right) M_{\text{dust}} \kappa_0 \left(\frac{\nu}{\nu_0} \right)^\beta [B_\nu(T_{\text{dust},z}) - B_\nu(T_{\text{CMB},z})]. \quad (4)$$

This equation, which depends on M_{dust} , $T_{\text{dust},z}$, β and potentially λ_{thick} in the optically thick scenario, will be used to fit the dust continuum emission of our high-redshift targets, as outlined in the following Section.

4.2 Modified Blackbody Fitting

In this work, we aim to simultaneously constrain the dust temperature and mass of three $z \approx 7$ galaxies through MBB fitting. Whilst we cannot robustly constrain β due to a lack of sampling of the dust SED, we explore various fixed values for β in the fits, and will additionally marginalize across β after choosing a suitable prior (see below).

We adopt the Monte Carlo Markov Chain (MCMC) algorithm implemented in Python library EMCEE (Foreman-Mackey et al. 2013)

¹ In what follows, flux densities are implied to be at observer-frame frequencies, such that the subscript “obs” is omitted.

Table 2. Physical and dust continuum properties of the three REBELS targets analyzed in this work.

ID ^a	RA ^b	DEC ^b	$z_{\text{[C II]}}^c$	$\log_{10}(M_{\star})^d$	$S_{\text{Band 6}}^e$	$S_{\text{Band 8}}$	$S_{\text{Band 8, tapered}}$
-	-	-	-	$\log_{10}(M_{\odot})$	μJy	μJy	μJy
REBELS-12	02:25:07.94	-05:06:40.70	7.3459 ± 0.0010	$9.94^{+0.32}_{-0.42}$	87 ± 24	$< 210^f$	-
REBELS-25	10:00:32.34	+01:44:31.11	7.3065 ± 0.0001	$10.27^{+0.10}_{-0.23}$	260 ± 22	486 ± 112	641 ± 147
REBELS-38	10:02:54.06	+02:42:12.12	6.5770 ± 0.0001	$10.37^{+0.15}_{-0.36}$	163 ± 23	-	334 ± 63
<i>REBELS-38 A</i>	10:02:54.08	+02:42:12.31	-	-	-	196 ± 45	-
<i>REBELS-38 B</i>	10:02:54.03	+02:42:12.11	-	-	-	165 ± 40	-

^aSource IDs listed in italic (with suffices *A*, *B*) denote the individual dust components labeled in Figure 1.

^bBand 8 dust continuum coordinates, except for the 88 μm -undetected REBELS-12, for which we quote Band 6 coordinates instead.

^c[C II]-based spectroscopic redshifts from Schouws et al. (in prep).

^dStellar masses from Topping et al. (2022), under the assumption of a non-parametric SFH.

^eALMA Band 6 (rest-frame 160 μm) continuum flux densities taken from Inami et al. (2022).

^fThe quoted upper limit is 3σ .

to fit the dust SEDs of the REBELS targets. We fit to the measured flux densities where available, and implement upper limits following the procedure described in Sawicki (2012) (see also Bakx et al. 2020; Witstok et al. 2022). In practice, we fit the logarithm of the dust mass $\log_{10}(M_{\text{dust}}/M_{\odot})$, for which we introduce a simple uniform prior of $\log_{10}(M_{\text{dust}}/M_{\odot}) \in [4, 10]$. The upper range of this prior is chosen to extend up to an unphysical value of $M_{\text{dust}}/M_{\star} \sim 1$, and we have explicitly verified that adopting a wider range does not affect our results. For $T_{\text{dust},z}$, we adopt a flat prior with a lower bound of $T_{\text{CMB},z}$, as we expect the dust to be at least as warm as the CMB. Given the wide variety observed in the dust temperatures of high-redshift galaxies (Section 6.2), we adopt a uniform prior between $T_{\text{CMB},z}$ and $T_{\text{dust,max}} = 150$ K, while beyond $T_{\text{dust,max}}$ we smoothly decrease the prior probability by a Gaussian with a width of $\sigma = 30$ K. This ensures that high-temperature solutions are not excluded a priori.²

For β we adopt a Gaussian prior centered around a mean of $\langle\beta\rangle = 1.8$ with a standard deviation of $\sigma_{\beta} = 0.5$, following the analysis of Faist et al. (2020) for four $z \sim 5.5$ galaxies. This value is consistent with that of local galaxies (Hildebrand 1983) and submillimeter galaxies (Da Cunha et al. 2021). However, we also use MBB fitting with a fixed value of $\beta = (1.5, 2.0)$. The latter value is similar to that of Milky Way dust ($\beta = 2.03$; Weingartner & Draine 2001; Draine 2003), which was assumed by Sommovigo et al. (2022a) to model the dust temperatures of REBELS targets with both a dust and a [C II] detection.

Two further remarks about the modified blackbody fitting routine are warranted, beginning with the implementation of upper limits. As per the Sawicki (2012) formalism, it is favourable for a model (that is, a MBB given some sampled $T_{\text{dust},z}$, M_{dust} and β) to be significantly below an upper limit rather than just below it. The reason is that, given a model with flux density f_{M} , an error of σ and an upper limit of 3σ , the log-likelihood $\ln \mathcal{L}$ is penalized by a factor of

$$\Delta \ln \mathcal{L} = \ln \left[\frac{1}{2} \left(1 + \operatorname{erf} \left(\frac{3\sigma - f_{\text{M}}}{\sqrt{2}\sigma} \right) \right) \right], \quad (5)$$

where $\operatorname{erf}(x)$ denotes the error function. Intuitively this can be understood as follows: when a model is just below the limiting flux, i.e., $f_{\text{M}} = 0.99 \times 3\sigma$, the probability of exceeding the flux limit given Gaussian noise is nearly 50%. As such, a model with $f_{\text{M}} \ll 3\sigma$ is preferred, given the decreased probability of exceeding the upper limit in the presence of noise. Nevertheless, this prescription does not exclude solutions which exceed the upper limit a priori, as any imposed limit may be exceeded with non-zero probability.

The second point is in reference to the fitting of modified blackbodies with a single detection and an upper limit. As per Equation 5, the solution that maximizes the log-likelihood is an MBB that matches the observed flux density, while simultaneously staying sufficiently far from the upper limit. In the case of REBELS-12, with a detection at rest-frame 158 μm and an upper limit at 88 μm , one such optimal solution will be a very cold MBB ($T_{\text{dust},z} \sim T_{\text{CMB},z} \approx 22$ K). However, MCMC ensures that (nearly) the full parameter space is explored, and as such allows for a variety of warmer MBB solutions that also accurately represent the data. This demonstrates that it is important to consider the full posterior distributions of the parameters of interest, and not only the maximum a posteriori solution (e.g., Hogg & Foreman-Mackey 2018). In this work, we therefore adopt the median of the posterior distributions as the fitted dust temperature, mass and emissivity, while the quoted errors represent the 16th and 84th percentiles of the corresponding posterior. We further remark that the posteriors of the fitted parameters are single-peaked in all cases (see also Appendix A).

We execute our MCMC routine with 32 walkers for a total of 10^5 steps each, thereby conservatively discarding the first 10^4 steps as the burn-in phase. We confirm that the number of samples utilized in the MCMC fitting is greater than $50\times$ the autocorrelation time to ensure sufficient sampling of the parameter space (e.g., Foreman-Mackey et al. 2013). The robustness of our fitting routine is further supported by the acceptance fractions obtained, averaging 0.33 across the three REBELS sources when β is fixed (1.5, 2.0), and 0.22 when β is included in the fitting (c.f., an optimal range of 0.2 – 0.5; Foreman-Mackey et al. 2013), and through the visual inspection of trace plots for M_{dust} , T_{dust} and β .

² We note that, when sampling dust temperatures that approach $T_{\text{CMB},z}$, the dust mass needed to match the observed flux densities rapidly increases, thereby potentially falling outside of our adopted prior range of $4.0 \leq \log(M_{\text{dust}}/M_{\odot}) \leq 10.0$. In practice, however, adopting this prior on M_{dust} comes down to excluding dust temperatures that approach the CMB temperature to within $\lesssim 0.1$ K. We have verified that the exclusion of this small fraction of the full parameter space does not affect the fits.

5 RESULTS

5.1 Dust Emission at $z \sim 7$

As outlined in Section 3, we detect Band 8 continuum emission (rest-frame $90 \mu\text{m}$) in two targets (REBELS-25 and REBELS-38), while the continuum is not detected in REBELS-12. In addition, all three targets were previously detected in Band 6 continuum (rest-frame $160 \mu\text{m}$; Inami et al. 2022). In what follows, we use our modified blackbody fitting routine to model the dust continuum SEDs of our targets in order to constrain their dust temperatures and masses. We first adopt an optically thin MBB, before considering optically thick dust.

5.1.1 Dust SED: Optically Thin Scenario

Given that high-redshift galaxies generally have a sparsely sampled dust SED, it is common in the literature to assume the dust is optically thin across the wavelength range of interest (e.g., Harikane et al. 2020; Bakx et al. 2021; Sugahara et al. 2021). As such, we proceed by fitting an optically thin MBB to our three REBELS targets, as shown in Figure 3. The top and middle rows show the fits for a fixed $\beta = 1.5$ and $\beta = 2.0$, respectively, while the bottom row shows the MBB fit using a Gaussian prior on β . In what follows, we adopt $\beta = 2.0$ as our fiducial model, to ensure consistency with the value assumed by Sommovigo et al. (2022a), and the series of REBELS papers in general.

We robustly constrain the dust temperatures of REBELS-25 and REBELS-38 using the high-S/N detection in Band 6 and the new Band 8 data. For REBELS-25, we find $T_{\text{dust},z} = 34 \pm 6 \text{ K}$, while for REBELS-38 we determine $T_{\text{dust},z} = 32^{+8}_{-5} \text{ K}$. In addition, we determine dust masses of $M_{\text{dust}} \approx 10^8 M_{\odot}$ for both targets (Table 3). We discuss these dust masses in the context of dust production mechanisms in Section 6.3.

Given the non-detection at Band 8 for REBELS-12 and the modest-S/N detection at Band 6, we cannot place robust constraints on its dust temperature, as the fitting allows for a long tail towards high temperatures (e.g., for $\beta = 2.0$ we find $T_{\text{dust},z} = 42^{+65}_{-14} \text{ K}$). We emphasize that in cases like REBELS-12, where strong observational constraints on the infrared SED are lacking, the inferred dust temperature depends strongly on the assumed prior. For example, doubling the prior range on the dust temperature to span $T_{\text{dust}} < 300 \text{ K}$ would result in the upper error on the dust temperature of REBELS-12 increasing by a factor of two as well. While the Band 8 upper limit for REBELS-12 is relatively constraining, the main uncertainty in our analysis is at present the S/N of the Band 6 data. For example, if we were to artificially reduce the uncertainty of its Band 6 flux density to obtain an S/N = 10, we would determine a low dust temperature of $T_{\text{dust},z} = 30^{+8}_{-5} \text{ K}$ for REBELS-12. However, with the current observations a higher temperature solution cannot be ruled out, as can be seen from the posterior distributions of $T_{\text{dust},z}$ in Appendix A. As detailed in Section 4, in this work we choose to place conservative priors on the dust temperature to avoid biasing the temperature measurements in cases where the constraining power of the data is weak. Hence, instead of artificially constraining the temperature measurements with narrower priors, obtaining high(er) quality multi-band observations is essential to accurately measure T_{dust} .

By propagating the full posterior distributions of the various MBB parameters determined through MCMC, we compute the infrared luminosities of our targets by integrating the sampled MBBs between rest-frame $8 - 1000 \mu\text{m}$. We measure an infrared luminosity of $\log_{10}(L_{\text{IR}}/L_{\odot}) = 11.36^{+0.23}_{-0.17}$ for REBELS-38, while for

REBELS-25 we determine $\log_{10}(L_{\text{IR}}/L_{\odot}) = 11.73^{+0.20}_{-0.18}$ given our fiducial $\beta = 2.0$. This value is lower than the infrared luminosity previously predicted for REBELS-25 by Sommovigo et al. (2022a) [$\log_{10}(L_{\text{IR}}/L_{\odot}) = 12.45^{+0.43}_{-0.45}$], using an estimate of $T_{\text{dust}}^{\text{S22a}} = 55^{+15}_{-14} \text{ K}$ based on its [C II] emission and underlying Band 6 continuum detection (see Appendix B for a more detailed comparison to single-band dust temperature models). Using our new Band 8 dust temperature measurement, we thus find that REBELS-25 may not be a ULIRG (c.f., Hygate et al. 2022). The continuum-detected REBELS sample therefore appears to consist solely of LIRGs, with $10^{11} \leq L_{\text{IR}}/L_{\odot} < 10^{12}$.

If we assume a lower $\beta = 1.5$, the inferred dust temperatures for the two sources detected in Band 8 continuum increase to $T_{\text{dust},z} \approx 40 - 45 \text{ K}$, with slightly larger uncertainties given that we now probe further redwards of the dust peak. Nevertheless, the inferred infrared luminosities do not significantly exceed ($< 0.2 \text{ dex}$) the values determined with the fiducial $\beta = 2.0$ due to the anticorrelation between dust temperature and dust mass. Indeed, the dust masses inferred when adopting $\beta = 1.5$ are lower compared to the fiducial model by $\sim 0.35 \text{ dex}$.³

When allowing for variation in β in the form of a Gaussian prior, we find similar temperatures of $\sim 40 \text{ K}$, though with 1σ uncertainties spanning a relatively wide range of $T_{\text{dust},z} \sim 30 - 65 \text{ K}$. The value of β itself is not constrained, and is correlated (anti-correlated) with the dust mass (temperature) as expected. As a result of this degeneracy between T_{dust} and β , a value of $\beta \approx 1.5$ is preferred by the fit. Intuitively, this can be understood as follows: given that we fit two ALMA measurements with three free parameters, the data can be (nearly) equally well represented by a family of models consisting of either a warm MBB with a shallow β , or a colder MBB with a steeper β . However, given $\beta = 1.8$ – the center of the adopted Gaussian prior – the dust temperature of our sources is found to be quite low ($T_{\text{dust}} > 40 \text{ K}$), leaving only a small parameter space of even colder MBBs, given that we require $T_{\text{dust},z} > T_{\text{CMB},z}$. Instead, given our high upper bound on $T_{\text{dust},z}$, a large number of equally good fits can be obtained with hotter dust and a shallower β . This naturally results in the median fitted β tending to shallower values, with T_{dust} increasing as a consequence. As such, while marginalizing across β results in more robust parameter uncertainties, we suggest the reader treat the fitted emissivity indices with some caution. An increased sampling of the continuum SED, in particular at longer wavelengths, is required to constrain the dust emissivity index more precisely.

5.1.2 Dust SED: Optically Thick Scenario

Given that the dust optical depth scales linearly with the dust surface density (Section 4), dust-rich galaxies may become optically thick at short wavelengths. Using a sample of 23 submillimeter galaxies (SMGs), Simpson et al. (2017) find a typical value for $\lambda_{\text{thick}} = 75^{+15}_{-20} \mu\text{m}$ given $\beta = 1.8$, though they caution this should be taken as a lower limit given that their results are based on observed galaxy sizes at longer wavelengths. Indeed, some particularly dusty sources are found to be optically thick to $\lambda_{\text{thick}} \approx 200 \mu\text{m}$ (Blain et al. 2003; Conley et al. 2011; Casey et al. 2019; Jin et al. 2022). However, making use of *Herschel* observations of local galaxies, Lutz et al.

³ Note, however, that while we here adopt a different value for β in the fit, we do not alter the normalization of the dust opacity $\kappa_0 = \kappa_{\nu}(1900 \text{ GHz})$. In practice, κ_0 and β are not independent, as both depend on the dust grain composition, as well as the grain size distribution (e.g., Bianchi 2013).

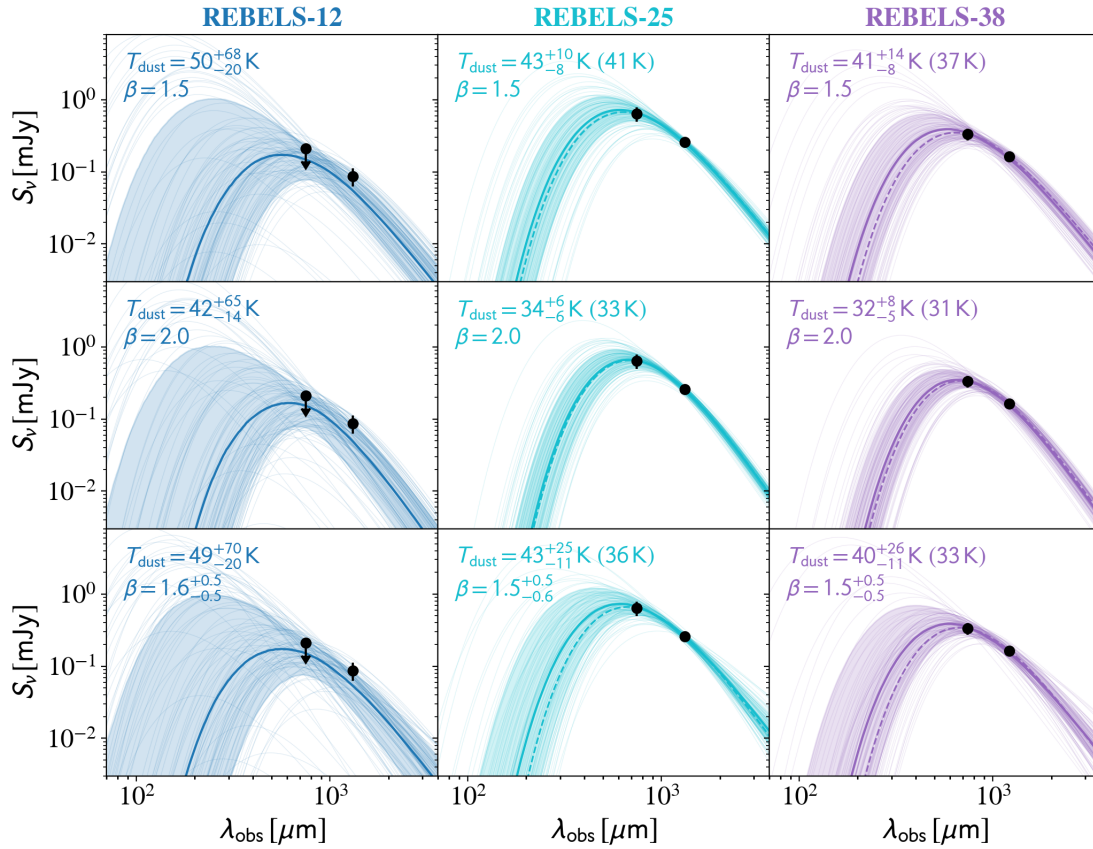


Figure 3. Optically thin MBB fits to REBELS-12, REBELS-25 and REBELS-38 using $\beta = 1.5$ (upper row), $\beta = 2.0$ (middle row) and a Gaussian prior on β (bottom row). The thick solid line shows the median SED obtained from the Monte Carlo samples, while the shaded region indicates the corresponding 1σ confidence interval. The dashed line shows the model using the fitting parameters that maximize the log-likelihood, and is omitted from the first column given that REBELS-12 is detected at only a single distinct frequency (Section 4). The median dust temperature and its corresponding uncertainty are indicated on the panel, with the maximum a posteriori value in parentheses. Individual semi-transparent lines represent randomly drawn Monte Carlo samples. Both sources with two continuum detections, REBELS-25 and REBELS-38, appear to have cold dust temperatures of $T_{\text{dust},z} \approx 30 - 35$ K given a fiducial $\beta = 2.0$. For REBELS-12, which is not detected in Band 8 and only at modest S/N in Band 6 ($\sim 3.6\sigma$ at $\lambda_{\text{obs}} \approx 1300 \mu\text{m}$), we cannot place strong constraints on $T_{\text{dust},z}$. However, the non-detection in Band 8 may imply a similarly modest dust temperature.

(2016) find that the majority of LIRGs are on average optically thin, while infrared-brighter sources may indeed be optically thick at far-infrared wavelengths.

In their analysis of the dust emission in $z \sim 4$ starburst GN-20, Cortzen et al. (2020) find the galaxy to be optically thick out to $\lambda_{\text{thick}} = 170 \pm 23 \mu\text{m}$ and determine its dust temperature to be $T_{\text{dust}} = 52 \pm 5$ K. However, they show that, had an optically thin MBB been assumed, the recovered dust temperature is substantially lower ($T_{\text{dust}} = 33 \pm 2$ K). As such, they clearly demonstrate that wrongfully adopting optically thin dust can significantly decrease the inferred dust temperatures.

For the REBELS targets studied in this work, we cannot fit λ_{thick} directly given that the dust SED is sampled at only two distinct wavelengths. However, we can determine a plausible value for λ_{thick} by assuming galaxies can be characterized by a spherical dust distribution of size R . In this case, the source is expected to become optically thick at a wavelength of

$$\lambda_{\text{thick}} = \lambda_0 \left(\frac{\pi R^2}{\kappa_0 M_{\text{dust}}} \right)^{-\frac{1}{\beta}} \approx 42 \mu\text{m} \times \left(\frac{R}{1 \text{kpc}} \right)^{-1} \left(\frac{M_{\text{dust}}}{10^8 M_{\odot}} \right)^{1/2}, \quad (6)$$

where the numerical value assumes $\beta = 2.0$. From our optically thin modified blackbody fitting, we infer a maximum dust mass of $M_{\text{dust}} \approx 10^8 M_{\odot}$ for our brightest target, REBELS-25. To obtain an estimate of λ_{thick} , we adopt this as a conservative upper limit on the true dust mass, given that, if the source is in fact optically thick, its true dust mass would be lower than inferred by optically thin models. For the size R , we adopt the median stacked continuum size of the dust-detected REBELS sample of $R = 1.1 \pm 0.3$ kpc (Fudamoto et al. 2022b). With these estimates, we expect $\lambda_{\text{thick}} \lesssim 40 \mu\text{m}$ to be a sensible upper limit on the wavelength where the dust transitions to optically thick. These calculations indicate that the REBELS sample is unlikely to be optically thick at the shortest wavelengths probed with ALMA of $\lambda_{\text{rest}} \approx 88 \mu\text{m}$.

Nevertheless, we investigate the effect of allowing for optically thick dust by adopting a fixed $\lambda_{\text{thick}} = 100 \mu\text{m}$ (following e.g., Faisst

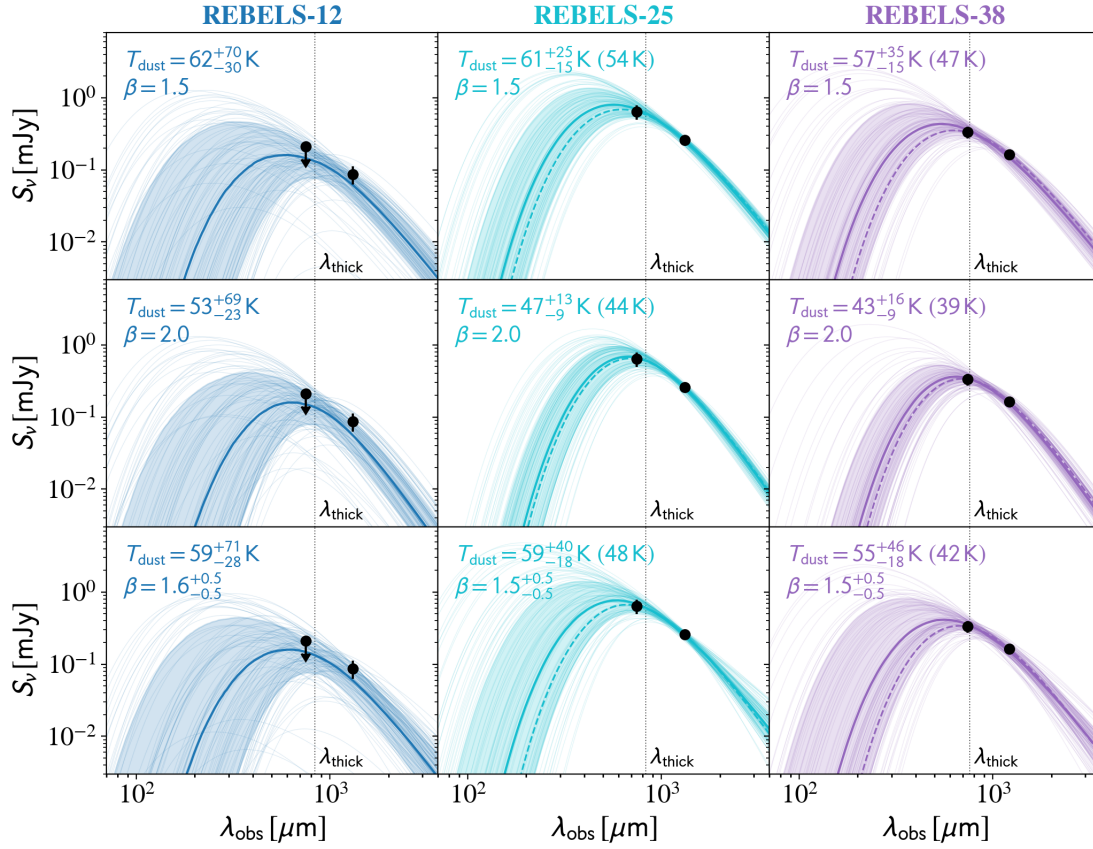


Figure 4. Same as Figure 3, now assuming an optically thick modified blackbody with a fixed $\lambda_{\text{thick}} = 100 \mu\text{m}$ to investigate how this affects the inferred temperatures. The observed-frame wavelength where the dust transitions from thin to thick is indicated through the dotted grey line. While we expect our sources to be optically thin beyond $\lambda \gtrsim 40 \mu\text{m}$ (Section 5.1.2), an optically thick scenario with $\lambda_{\text{thick}} = 100 \mu\text{m}$ would result in higher inferred dust temperatures by $\Delta T_{\text{dust}} \sim 10 - 15 \text{ K}$.

Table 3. Dust parameters derived from modified blackbody fitting. Optically thick MBB fitting assumes a fixed $\lambda_{\text{thick}} = 100 \mu\text{m}$. The dust emissivity is kept fixed to either $\beta = 1.5, 2.0$ (top and middle rows), or is marginalized across using a Gaussian prior (bottom row; see text).

	REBELS-12		REBELS-25		REBELS-38	
Optical Depth:	Thin	Thick	Thin	Thick	Thin	Thick
β	1.5	1.5	1.5	1.5	1.5	1.5
$\log_{10}(M_{\text{dust}}/M_{\odot})$	$6.94^{+0.92}_{-0.94}$	$6.87^{+0.88}_{-0.69}$	$7.80^{+0.30}_{-0.26}$	$7.54^{+0.30}_{-0.30}$	$7.56^{+0.35}_{-0.37}$	$7.31^{+0.37}_{-0.45}$
$T_{\text{dust}} [\text{K}]$	50^{+68}_{-20}	62^{+70}_{-30}	43^{+10}_{-8}	61^{+25}_{-15}	41^{+14}_{-8}	57^{+35}_{-15}
$\log_{10}(L_{\text{IR}}/L_{\odot})$	$11.34^{+1.12}_{-0.49}$	$11.31^{+0.73}_{-0.47}$	$11.84^{+0.28}_{-0.23}$	$11.95^{+0.36}_{-0.27}$	$11.48^{+0.34}_{-0.23}$	$11.59^{+0.47}_{-0.27}$
β	2.0	2.0	2.0	2.0	2.0	2.0
$\log_{10}(M_{\text{dust}}/M_{\odot})$	$7.10^{+0.94}_{-1.23}$	$6.97^{+0.91}_{-0.86}$	$8.13^{+0.37}_{-0.26}$	$7.78^{+0.29}_{-0.26}$	$7.90^{+0.39}_{-0.35}$	$7.58^{+0.35}_{-0.38}$
$T_{\text{dust}} [\text{K}]$	42^{+65}_{-14}	53^{+69}_{-23}	34^{+6}_{-6}	47^{+13}_{-9}	32^{+8}_{-5}	43^{+16}_{-9}
$\log_{10}(L_{\text{IR}}/L_{\odot})$	$11.28^{+1.19}_{-0.40}$	$11.21^{+0.71}_{-0.38}$	$11.73^{+0.20}_{-0.18}$	$11.77^{+0.23}_{-0.19}$	$11.36^{+0.23}_{-0.17}$	$11.40^{+0.27}_{-0.18}$
β	$1.6^{+0.5}_{-0.5}$	$1.6^{+0.5}_{-0.5}$	$1.5^{+0.5}_{-0.6}$	$1.5^{+0.5}_{-0.5}$	$1.5^{+0.5}_{-0.5}$	$1.5^{+0.5}_{-0.5}$
$\log_{10}(M_{\text{dust}}/M_{\odot})$	$6.94^{+0.95}_{-0.95}$	$6.89^{+0.90}_{-0.73}$	$7.81^{+0.47}_{-0.47}$	$7.58^{+0.38}_{-0.41}$	$7.59^{+0.52}_{-0.56}$	$7.34^{+0.45}_{-0.51}$
$T_{\text{dust}} [\text{K}]$	49^{+70}_{-20}	59^{+71}_{-28}	43^{+25}_{-11}	59^{+40}_{-18}	40^{+26}_{-11}	55^{+46}_{-18}
$\log_{10}(L_{\text{IR}}/L_{\odot})$	$11.33^{+1.09}_{-0.47}$	$11.27^{+0.75}_{-0.44}$	$11.85^{+0.39}_{-0.24}$	$11.92^{+0.49}_{-0.28}$	$11.47^{+0.46}_{-0.23}$	$11.56^{+0.56}_{-0.28}$

et al. 2020; Da Cunha et al. 2021). In the observed frame, this corresponds to $\lambda_{\text{thick}} \approx 760 - 830 \mu\text{m}$ for our three targets, implying non-negligible optical depth effects in ALMA Band 8. We caveat that, since $\tau_{\nu} \propto \Sigma_{\text{dust}}$, this necessarily implies significant dust surface densities due to large overall dust masses and/or compact dust-obscured star-forming regions (Equation 6). In these scenarios, nearly all of the UV emission associated with star formation will be attenuated by dust. However, since the REBELS targets were explicitly selected to be UV-bright galaxies, reconciling this with a high dust optical depth requires spatial offsets between the dust and UV emission, or clumpy dust substructures (e.g., Behrens et al. 2018; Ferrara et al. 2022).

The optically thick MBB fits assuming $\lambda_{\text{thick}} = 100 \mu\text{m}$ are shown in Figure 4. The inferred temperatures exceed the ones determined using optically thin models by $\Delta T_{\text{dust}} \approx 10 - 15 \text{ K}$, while dust masses are found to be lower than in our fiducial analysis by $\sim 0.25 \text{ dex}$ (Table 3). Nevertheless, the inferred infrared luminosities, and therefore the corresponding dust-obscured star formation rates, are consistent with the ones derived from optically thin MBB fitting within the uncertainties. We note that, had we assumed $\lambda_{\text{thick}} = 40 \mu\text{m}$ based on the aforementioned estimate for REBELS (Equation 6), the inferred temperatures agree with the optically thin ones to within $\lesssim 2 \text{ K}$ ($\lesssim 4 \text{ K}$) for $\beta = 2.0$ ($\beta = 1.5$).

5.1.3 The Dust Morphology of REBELS-38

In the moderate resolution Band 8 imaging of $0''.61 \times 0''.48$, REBELS-38 is resolved into two components detected at a peak significance of 4.3 and 4.1σ . While unresolved in the original REBELS Band 6 observations, Inami et al. (2022) noted an offset between the peaks of its rest-frame UV and dust continuum emission of $0''.57 \pm 0''.25$, corresponding to a physical offset of $3.1 \pm 1.4 \text{ kpc}$. In the higher resolution Band 8 data, we observe that the fainter clump (B) is nearly co-spatial with the UV emission (offset of $0.9 \pm 0.4 \text{ kpc}$), while clump A is offset to the east by $4.0 \pm 0.4 \text{ kpc}$. The separation between the two clumps themselves equals $0''.73 \pm 0''.11$ ($4.0 \pm 0.6 \text{ kpc}$), and both are spatially unresolved individually ($r_{1/2} < 1.5 \text{ kpc}$). Given the small separation between the clumps, it is likely that these are individual components of a singular galaxy, although we note the possibility that REBELS-38 could be a late-stage merger.

5.2 [O III] Emission

Given the known [C II]-based spectroscopic redshifts of REBELS-12 and REBELS-25, we search for and detect the [O III] line in the Band 8 datacubes. The extracted 1D spectra of the [O III] emission are shown in the top row of Figure 5. We fit the spectra with a Gaussian profile, and determine the total line flux by integrating the area under the Gaussian curve. The line fluxes, luminosities and FWHMs are listed in Table 4.

In the bottom row of Figure 5, we compare to the [C II] emission lines for our sources (Schouws et al. in prep), adopting $v = 0 \text{ km s}^{-1}$ as the center of the [C II] line, given its higher S/N compared to [O III]. In what follows, we discuss the emission line properties and morphologies of both sources targeted in [O III] emission in detail.

5.2.1 REBELS-12

Intriguingly, the [C II] line in REBELS-12 is very broad, with a FWHM $\approx 640 \text{ km s}^{-1}$, while the [O III] emission is comparatively narrow, FWHM $\approx 130 \text{ km s}^{-1}$. Moreover, the [C II] emission appears

to consist of two peaks separated by $\Delta v \sim 500 \text{ km s}^{-1}$, indicating that REBELS-12 may be a merger, although it could also be a signature of disk rotation (e.g., Kohandel et al. 2019). The velocity of the [O III] emission coincides with the redder peak, while no counterpart to the bluer emission is visible in the [O III] spectrum.

We proceed by quantitatively investigating this line profile. We first fit the one-dimensional [C II] spectrum of REBELS-12 with two Gaussian components, as shown in the top panel of Figure 6. The blue and red components each contain a flux of $S_{[\text{C II}]}^{\text{blue}} = 443_{-130}^{+237} \text{ mJy km s}^{-1}$ and $S_{[\text{C II}]}^{\text{red}} = 358_{-186}^{+141} \text{ mJy km s}^{-1}$, respectively. The total flux across the two Gaussians is consistent with that obtained from the single-Gaussian fit, as reported in Table 4.

We subsequently image the channels corresponding to the FWHMs of the blue and red Gaussians separately, and show the contours on top of stacked JHK-imaging and [O III] emission (Figure 6; bottom panel). The redder Gaussian component is co-spatial with both the [O III] and rest-frame UV emission, while the peak of the blue component is offset to the southwest by $\sim 1''$. This may indicate that REBELS-12 is a merger, consisting of a UV-bright component emitting in [O III] and a faint galaxy with no discernible UV or dust continuum emission. This scenario is particularly appealing given that a serendipitous, UV-dark galaxy was previously found $\sim 11''.5$ away from REBELS-12 by Fudamoto et al. (2021), implying that REBELS-12 may be part of a larger cosmic structure at $z \approx 7.3$.

Assuming REBELS-12 is indeed a merging galaxy, we infer a line ratio for the red component of $[\text{O III}]/[\text{C II}] = 3.3_{-1.0}^{+3.3}$. For the blue component, we can only place an upper limit on the emission line ratio. We assume its [O III] FWHM is equal to that of the observed red component and adopt a peak line flux of $3\times$ the RMS across the FWHM (corresponding to the RMS in a 130 km s^{-1} channel). We then infer an upper limit of $S_{[\text{O III}]}^{\text{blue}} \lesssim 280 \text{ mJy km s}^{-1}$, and a line ratio of $[\text{O III}]/[\text{C II}] < 1.1$ for the blue component. In contrast, if we treat REBELS-12 as a singular system, we determine $[\text{O III}]/[\text{C II}] = 1.5_{-0.5}^{+1.0}$ (Table 4).

Finally, we highlight the peculiar dust morphology of REBELS-12. As detailed in Inami et al. (2022), its dust emission at rest-frame $160 \mu\text{m}$ shows two separate components, the brightest of which is spatially offset from the (red component of the) [C II] and [O III] emission, as well as from the UV emission (Figure 2). It is possible that this dust component corresponds to a foreground source that is not physically related to REBELS-12, although at present there is no known counterpart at shorter wavelengths. However, deeper and higher resolution ALMA observations of REBELS-12 are required to better understand the nature of its [C II], [O III] and dust emission.

5.2.2 REBELS-25

For REBELS-25, we find that the [O III] emission is slightly blueshifted compared to the [C II] emission by $\Delta v = -60 \pm 15 \text{ km s}^{-1}$. Similar to what we observe for REBELS-12, the [O III] line is narrower than the [C II] emission. However, given the signal-to-noise ratio and resolution of the existing data, we do not find evidence for significant spatial offsets between the dust continuum and the emission lines in REBELS-25. Its [C II] line is characterized by a double-peaked component and the corresponding velocity field has been shown to resemble that of a rotating disk (Hygate et al. 2022). High-resolution ALMA follow-up observations of the [C II] line have confirmed this, and will be described in a dedicated publication (Rowland et al. in prep). The larger linewidth of the [C II] line therefore likely implies it traces an extended gas reservoir at larger circular velocities than the [O III] emission. We adopt the [C II] line

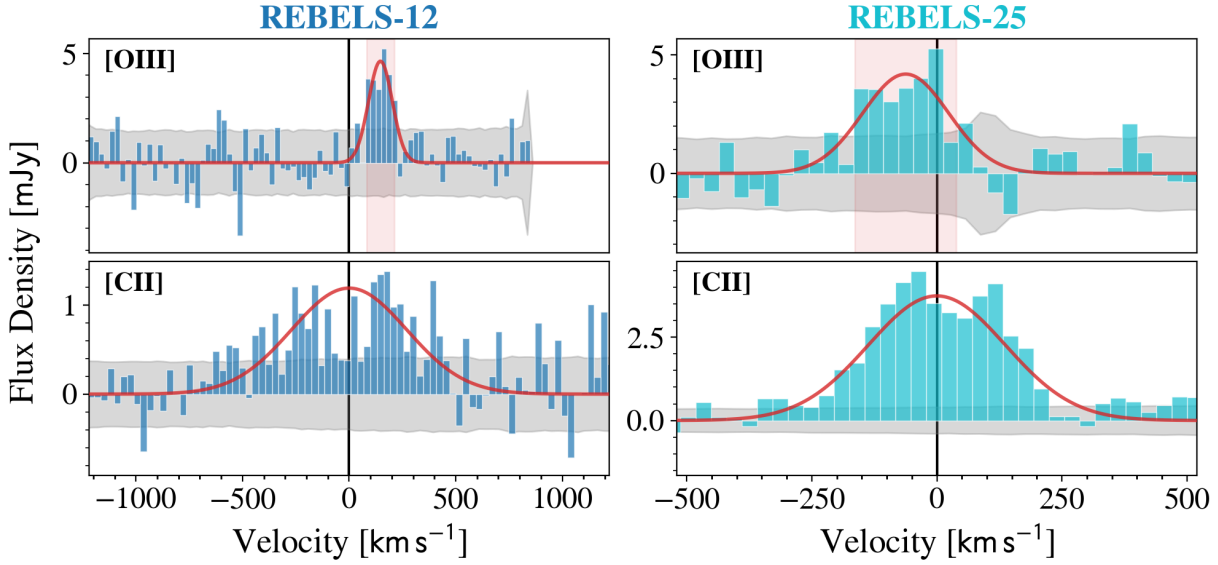


Figure 5. The extracted [O III] (top) and [C II] emission (bottom) for REBELS-12 (left) and REBELS-25 (right). The grey band shows the noise level per channel and the red line represents a Gaussian fit to the spectrum. The red shading corresponds to the FWHM of the [O III] line, across which we collapse the channels to create the moment-0 map. The black vertical line corresponds to the center of the [C II] line, defined to be at $v = 0$. In both sources, the [C II] line is broader than the [O III] emission, although there is tentative evidence that the [C II] emission in REBELS-12 consists of two components, one of which is blueshifted by $\sim 500 \text{ km s}^{-1}$ compared to the observed [O III] emission (see text). Adopting the total line fluxes for both emission lines, we find $[\text{O III}]/[\text{C II}] \approx 1 - 1.5$ in both galaxies.

Table 4. Emission line properties of REBELS-12 and REBELS-25.

ID	$z_{[\text{O III}]}$	$S_{[\text{O III}]}$	$\text{FWHM}_{[\text{O III}]}$	$L_{[\text{O III}]}$	$S_{[\text{C II}]}$ ^a	$\text{FWHM}_{[\text{C II}]}$ ^a	$L_{[\text{C II}]}$ ^a	$L_{[\text{O III}]} / L_{[\text{C II}]}$
		mJy km s^{-1}	km s^{-1}	$10^8 L_{\odot}$	mJy km s^{-1}	km s^{-1}	$10^8 L_{\odot}$	
REBELS-12	7.3491 ± 0.0002	654^{+149}_{-133}	130 ± 21	$14.6^{+3.5}_{-2.9}$	807 ± 155	637 ± 82	10.1 ± 4.1	$1.5^{+1.0}_{-0.5}$
REBELS-25	7.3052 ± 0.0004	896^{+234}_{-207}	203 ± 38	$20.0^{+5.1}_{-4.6}$	1280 ± 36	322 ± 12	15.9 ± 1.0	1.3 ± 0.3

^a[C II] fluxes, FWHMs and luminosities from Schouws et al. (in prep).

luminosity for REBELS-25 determined by Schouws et al. (in prep) and determine its line ratio to be $[\text{O III}]/[\text{C II}] = 1.3 \pm 0.3$.

While the [C II] emission in distant galaxies has been observed to generally be more spatially extended than the [O III] emission (e.g., Carniani et al. 2020; Akins et al. 2022; Section 6.1), we note that our results remain unchanged if we re-extract the [C II] fluxes following the procedure adopted for the [O III] line described in Section 3. This is as expected, given that the fluxes are extracted in an aperture with a radius of $\sim 10 \text{ kpc}$ at $z = 7$, which is much larger than the typical [C II] sizes of galaxies of $r_{[\text{C II}]} \sim 2 \text{ kpc}$ (Fujimoto et al. 2020; Fudamoto et al. 2022b). In addition, we verified that our method of extracting the spectra across only the pixels with $\text{SNR} > 2$ in the moment-0 map (Section 3) does not appreciably affect the measured [O III] line fluxes. If we instead extract the flux across all pixels in a circular aperture larger than the synthesized beam, we find that the measured line fluxes increase by factor of $0.8^{+0.5}_{-0.4}$ and $1.5^{+0.7}_{-0.6}$ for REBELS-12 and REBELS-25, respectively (using apertures with radii of $1''.0$ and $1''.25$). This is consistent with our fiducial measurements to within 1σ , and hence suggests we are unlikely to miss significant extended [O III] emission.

6 DISCUSSION

We proceed by first discussing the physical properties of our targets in terms of the [O III]/[C II] emission line ratio, and subsequently link these to their dust continuum properties in the sections that follow.

6.1 [O III]/[C II] as a Proxy for Burstiness

The ratio between the [O III] and [C II] luminosities provides a global characterization of the ISM. This line ratio is observed to have typical values of $\lesssim 1$ in starbursts at $z \sim 0$ (Díaz-Santos et al. 2017), while generally being $\geq 2 - 10$ in high-redshift galaxies ($z \gtrsim 6$; Harikane et al. 2020). This may be indicative of an increasingly ionized ISM at early cosmic times, although alternative interpretations, such as low metallicities and/or low C/O abundance ratios, have also been proposed as a means to increase the relative [O III]/[C II] emission of high-redshift galaxies (e.g., Arata et al. 2020; Katz et al. 2022).

Combining a sample of three newly observed $z \approx 6$ Lyman Break Galaxies with six $6 \lesssim z \lesssim 9$ galaxies from the literature, Harikane et al. (2020) find the line ratios to span a broad range of

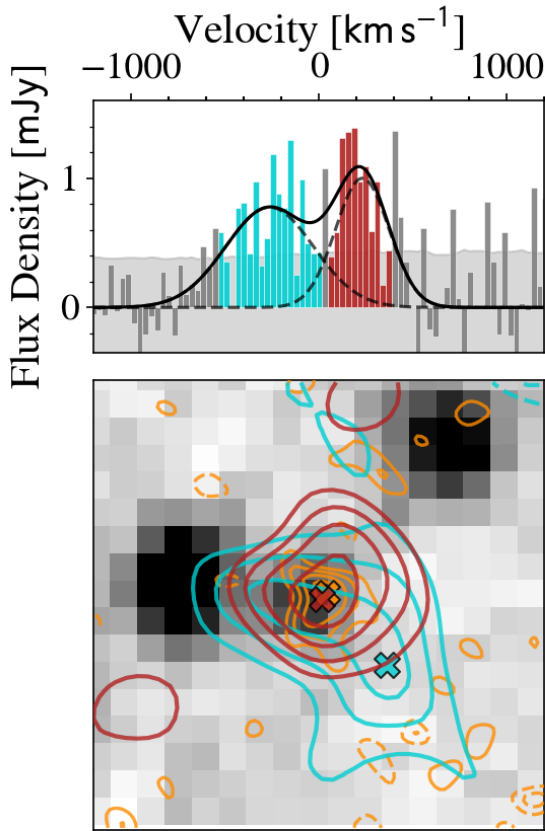


Figure 6. Upper: double-Gaussian fit to the [C II] line profile of REBELS-12. The channels highlighted in blue and red are imaged separately, and are shown as contours (starting at 2σ in steps of 1σ) in the **lower** panel. The [O III] contours are additionally overplotted in orange. The emission peaks of the individual components are indicated via crosses. The red Gaussian is co-spatial with the rest-frame UV and [O III] emission, while the blue Gaussian appears extended, being both spectrally and spatially offset from the red component. While higher resolution imaging is needed to confirm its nature, current observations suggest REBELS-12 may be a merger of a UV-bright component – additionally emitting in [C II] and [O III] – and a UV-dark component visible only in [C II] emission.

$[\text{O III}]/[\text{C II}] = 2 - 20$.⁴ While [Carniani et al. \(2020\)](#) show that some [C II] emission may be missed due to surface brightness dimming, given the typically larger extent of [C II] compared to [O III], even upon accounting for this, they still find line ratios greater than unity ($[\text{O III}]/[\text{C II}] = 2 - 8$) for the same nine $z > 6$ galaxies analyzed by [Harikane et al. \(2020\)](#). This is in agreement with recent measurements from [Witstok et al. \(2022\)](#) for five additional galaxies at $z \approx 7$ detected in both [C II] and [O III] emission, for which they similarly find the line ratios to span $[\text{O III}]/[\text{C II}] \sim 2 - 8$. In addition, [Akins et al. \(2022\)](#) find a ratio of $[\text{O III}]/[\text{C II}] \sim 2$ for A1689-zD1 at $z = 7.13$, when adopting an aperture large enough to include the [C II] emission from the extended halo around the source.

Through detailed CLOUDY ([Ferland et al. 1998, 2017](#)) modelling,

⁴ Their literature sample comprises MACS1149-JD1 ([Hashimoto et al. 2018](#)), A2744-YD4 ([Laporte et al. 2017](#)), MACS0416-Y1 ([Tamura et al. 2019](#); [Bakx et al. 2020](#)), SXDF-NB1006-2 ([Inoue et al. 2016](#)), The Big Three Dragons ([Hashimoto et al. 2019](#)) and BDF-3299 ([Carniani et al. 2017](#)).

[Harikane et al. \(2020\)](#) find that the large [O III]/[C II] ratios observed in high-redshift galaxies are likely due to A) a high ionization parameter U_{ion} , and/or B) a low PDR covering fraction, while other effects, such as metallicity, C/O abundance, and ISM density are subdominant. Both of these scenarios involve suppressing the [C II] luminosity: at fixed metallicity and density, the [C II] luminosity decreases for a larger U_{ion} as C^+ becomes increasingly ionized ([Harikane et al. 2020](#); their Figure 11). Similarly, as most of the [C II] emission is believed to emanate from PDRs (e.g., [Cormier et al. 2019](#)), a lower PDR covering fraction also decreases the overall [C II] luminosity.

Our sample of three $z \approx 7$ galaxies, on the other hand, shows [C II] line luminosities consistent with the local relation between [C II] luminosity and SFR ([Schouws et al. in prep](#)). While [O III] observations exist only for REBELS-12 and REBELS-25, the inferred global line ratios ($[\text{O III}]/[\text{C II}] \approx 1.3 - 1.5$; Figure 7) are indicative of less extreme physical conditions in our targets compared to the known $z \geq 6$ population. Instead, our targets show line ratios consistent with the upper range inferred for local (U)LIRGs ([Díaz-Santos et al. 2017](#)). However, we note that if we instead treat REBELS-12 as a merging system, its [O III]-bright component shows an [O III]/[C II] ratio that is similar to that of the $z \geq 6$ literature sample, while the upper limit obtained for the [O III]-faint component suggests it has a line ratio lower than the known high-redshift population.

The line ratios determined for REBELS-12 and REBELS-25 are additionally consistent with the sample of ~ 200 simulated galaxies analyzed by [Pallottini et al. \(2022\)](#). These galaxies are drawn from the cosmological zoom-in simulations SERRA at $z = 7.7$, which are post-processed in order to obtain galaxy UV, FIR and line luminosities. While the SERRA sample mostly probes galaxies with $\text{SFR} \sim 1 - 10 M_{\odot} \text{ yr}^{-1}$ – lower than currently accessible with observations of unlensed galaxies such as REBELS – the agreement between the simulations and observations is nonetheless encouraging.

In what follows, we investigate the origin of the different [O III]/[C II] ratios seen in our REBELS targets and the previously observed $z \geq 6$ population quantitatively in the context of the ionization parameter, which [Harikane et al. \(2020\)](#) show is the dominant ingredient governing the [O III]/[C II] emission line ratio. While in practice there is a degeneracy between a lower/higher ionization parameter and higher/lower PDR covering fraction, we here focus on the former scenario. As discussed in [Harikane et al. \(2020\)](#), a low PDR covering fraction would allow for the efficient transmission of ionizing photons, and can therefore be independently investigated through Lyman- α spectroscopy. Keck/MOSFIRE observations of REBELS-12 and REBELS-25, however, do not reveal a Lyman- α detection for these two $z \sim 7.3$ targets ([Algera et al. in prep](#)).

As shown by [Ferrara et al. \(2019\)](#), the ionization parameter is related to the star formation rate and molecular gas surface densities via $U_{\text{ion}} \propto \Sigma_{\text{SFR}}/\Sigma_{\text{gas}}^2$. Defining the parameter κ_s as the offset from the local Schmidt-Kennicutt relation via $\Sigma_{\text{SFR}} = \kappa_s \Sigma_{\text{gas}}^{1.4}$, [Ferrara et al. \(2019\)](#) rewrite the ionization parameter as $U_{\text{ion}} \propto \kappa_s^{1.4} \Sigma_{\text{SFR}}^{-0.4}$. As a result, large values of the [O III]/[C II] ratio may be related to high values of the “burstiness” κ_s , corresponding to large upward deviations from the local Schmidt-Kennicutt relation.

We next adopt the models introduced by [Vallini et al. \(2021\)](#) to relate the observed emission line ratios to the burstiness of our sources. Their framework, dubbed GLAM,⁵ takes the [O III], [C II] and star formation rate surface densities as inputs and uses these to constrain the burstiness, metallicity and ISM density through a

⁵ https://vallini.github.io/MCMC_galaxyline_analyzer/

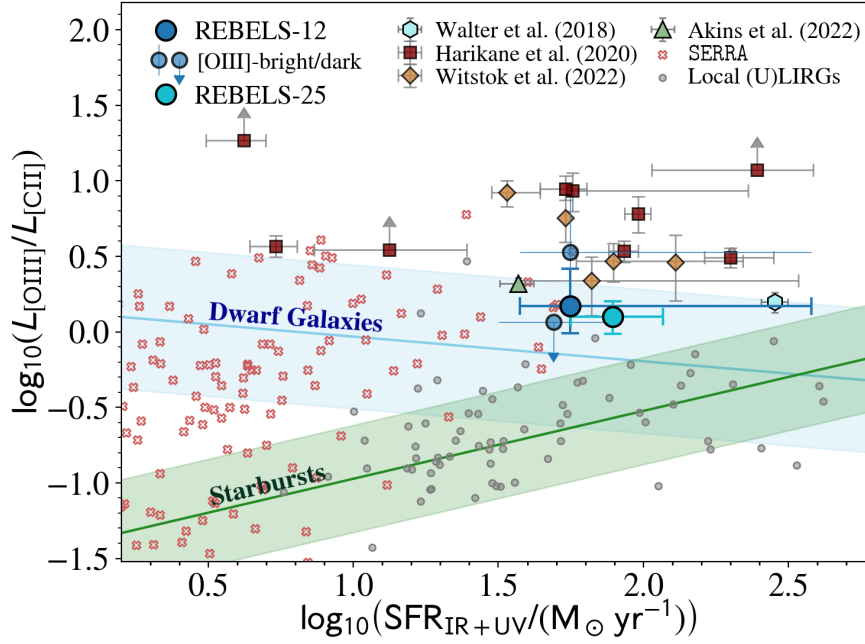


Figure 7. The [O III]/[C II] luminosity ratio versus total (IR + UV) star formation rate for REBELS-12, REBELS-25 and a variety of galaxies in the literature. Given that REBELS-12 could be a merger of an [O III]-bright and [O III]-dark galaxy (Sec. 5.2.1), we show both its [O III]/[C II] ratio for the two individual components, and for the system as a whole. We assign the UV-dark component a star formation rate based on its [C II] emission, using the relation from Schaefer et al. (2020), while for the total system we adopt the SFR from its combined UV and infrared emission. The compilation of nine $6 \lesssim z \lesssim 9$ galaxies from Harikane et al. (2020) is shown as maroon squares, while the five $z \sim 7$ galaxies from Witstok et al. (2022) are plotted as orange diamonds. We additionally show the $z = 7.13$ galaxy A1689-zD1 recently analyzed by Akins et al. (2022) and the $z = 6.08$ quasar companion from Walter et al. (2018). The $z \sim 0$ GOALS (U)LIRGs from Díaz-Santos et al. (2017) are shown as grey dots, and the local relations for starburst and dwarf galaxies from De Looze et al. (2014) are indicated through the green and blue bands, respectively. In addition, we show the $z = 7.7$ galaxies from the SERRA simulation suite (Pallottini et al. 2022) through the pink crosses. Compared to the $z \gtrsim 6$ population, REBELS-12 and REBELS-25 show lower [O III]/[C II] ratios.

Monte Carlo-based approach. In order to determine the required line and IR surface densities, we define $\Sigma_{\text{line}} = L_{\text{line}} / (2\pi r_{\text{line}}^2)$, where r is the source radius measured in the image plane and “line” refers to either [C II] or [O III], and $\Sigma_{\text{IR}} = L_{\text{IR}} / (2\pi r_{\text{IR}}^2)$. We determine the galaxy sizes of the different components through image plane fitting with a 2D Gaussian, and quote circularized radii, defined as $r = \sqrt{ab}/2$ where a, b are the FWHM of the major and minor axes, respectively. Given the moderate resolution of our data, we further assume a fiducial 30% uncertainty on all of the size measurements when utilizing them in the Vallini et al. (2021) models.

For REBELS-12, both emission lines are spatially resolved, and we adopt $r_{\text{[C II]}} = 3.8 \pm 1.1$ kpc and $r_{\text{[O III]}} = 1.5 \pm 0.4$ kpc. The Band 6 continuum emission is additionally resolved, but shows a complex morphology (Section 5.2 and Figure 2). In particular, at present it remains unclear if both dust components are physically associated to REBELS-12, or whether the brighter one corresponds to a foreground object. We here conservatively adopt the combined flux density of the two dust components, while adopting a compact size of $r_{\text{IR}} = r_{\text{[O III]}}$ for REBELS-12. This ensures that we effectively determine an upper limit on its true burstiness, which will strengthen our subsequent claims that the REBELS sources are less bursty than the known $z \gtrsim 6$ population (Section 6.4). We additionally run the models for just the [O III]-bright component of REBELS-12, corresponding to the red [C II] component in Figure 6, for which we measure a size of $r_{\text{[C II]}} = 2.6 \pm 0.8$ kpc.

For REBELS-25, we only find the Band 6 continuum to be resolved (Inami et al. 2022). Based on a 2D Gaussian fit, we determine $r_{\text{IR}} =$

1.8 ± 0.5 kpc, and we adopt an identical size for the unresolved [O III] emission. The [C II] emission is similarly not resolved, such that the beam size translates to a robust upper limit on its [C II] size of $r_{\text{[C II]}} < 3.7$ kpc. Given the general observation among high-redshift galaxies that [C II] is more extended than the dust continuum (e.g., Carniani et al. 2020), we therefore adopt a fiducial size of $r_{\text{[C II]}} = 3.0 \pm 0.9$ kpc for REBELS-25, in agreement with the findings by Fudamoto et al. (2022b) that the [C II] sizes of the REBELS sources are $\sim 2\times$ larger than their dust continuum sizes.

Based on the inferred line luminosities and galaxy sizes, we determine the corresponding surface densities which we provide as inputs to GLAM. Treating REBELS-12 as a singular system by using its total [C II] luminosity, we measure a burstiness parameter of $\kappa_s = 13.5^{+7.9}_{-5.4}$, while finding a slightly larger $\kappa_s = 19.0^{+9.8}_{-7.3}$ when adopting only the [C II] emission that is co-spectral with the [O III] line. For REBELS-25, we infer a burstiness parameter of $\kappa_s = 17.8^{+11.1}_{-6.8}$. These values are on the low end of the burstiness of $\kappa_s = 10 - 100$ (average of $\kappa_s \sim 40$) inferred among the sample of nine high-redshift galaxies analyzed by Vallini et al. (2021), while being slightly larger than, but overall consistent with, the median burstiness of the simulated SERRA galaxies at $z = 7.7$ of $\kappa_s = 6.5^{+11.5}_{-4.0}$ (Pallottini et al. 2022).

We relate the inferred burstiness to the global physical properties of our REBELS targets in Section 6.2, and we utilize them in the context of single-band dust temperature modelling in Appendix B. There we show that the temperatures predicted from the Sommovigo et al. (2022a) single-band dust models are in agreement with those

obtained from MBB-fitting, when adopting appropriate priors on the burstiness. In addition, in Appendix B we show that the fitted temperatures agree with those predicted by the single-band models from Inoue et al. (2020) and Fudamoto et al. (2022a).

6.2 Dust Temperatures at High Redshift

Since the advent of ALMA, considerable effort has been dedicated to constraining the dust temperatures of individual galaxies in the epoch of reionization, in order to get an accurate census of their dust-obscured star formation rates, and to constrain models of dust build-up in the early Universe. While it remains unclear if, and to what extent, average dust temperatures evolve with redshift, what is clear from observations of individual sources at $z \gtrsim 6$ is that the scatter in T_{dust} is large. This is illustrated by the low temperature of $T_{\text{dust}} \sim 30$ K found for COS-3018555981 at $z \sim 7$ by Witstok et al. (2022), and the existence of two sources at $z \sim 8$ with dust temperatures in excess of 80 K (Laporte et al. 2017; Behrens et al. 2018; Bakx et al. 2020). However, the set of high-redshift galaxies with multi-band ALMA photometry is very inhomogeneous, and any comparisons across the literature sample are further complicated by the adoption of different fitting techniques and priors.⁶ In order to fairly compare the REBELS targets analyzed in this work to the literature, we therefore compile the observed continuum flux densities for all $z \gtrsim 5$ normal star-forming galaxies targeted at a minimum of two distinct ALMA bands with at least one of those being a continuum detection at $> 3\sigma$. For galaxies not detected in a given band, an upper limit of $3\times$ the RMS is adopted instead. This results in a sample of thirteen galaxies (listed in Table CI in the Appendix), eight of which are detected in continuum emission in two or more bands (at $> 3\sigma$). This literature sample includes four galaxies at $z \sim 5.5$ from Faisst et al. (2020), two galaxies at $z \sim 6$ from Harikane et al. (2020) (see also Ono et al. 2022), three sources at $z \sim 7$ from Witstok et al. (2022), the Big Three Dragons at $z = 7.15$ (Hashimoto et al. 2019; Sugahara et al. 2021), A1689-zD1 at $z = 7.13$ (Bakx et al. 2021; Akins et al. 2022), A2744-YD4 at $z = 7.88$ (Laporte et al. 2017, 2019; Morishita et al. 2022) and MACS0416-Y1 at $z = 8.31$ (Bakx et al. 2020).⁷ We note that the last three sources are gravitationally lensed galaxies. In what follows, we adopt our fiducial model of optically thin dust with $\beta = 2.0$ for the REBELS and $z \gtrsim 5$ literature samples. However, we note that our results are qualitatively consistent when a different fixed value of β is adopted.

We show the dust temperatures of the REBELS and literature sources as a function of redshift in Figure 8. We additionally overplot sources at low and intermediate redshifts analyzed by Schreiber et al. (2018), adopting the dust temperatures directly from their work (see also Sommovigo et al. 2022a).

The REBELS sources analyzed in this work are on average characterized by colder dust ($T_{\text{dust}} \sim 30 - 35$ K) than the $z \sim 7$ literature sources used for comparison. By concatenating the posterior T_{dust} probability density functions of our REBELS targets (c.f., Figure A1), we determine a median dust temperature of $\langle T_{\text{dust},z} \rangle = 34^{+14}_{-7}$ K

⁶ For example, different studies adopt different values of β , different priors on T_{dust} , and different definitions of ‘best fit’ (e.g., maximum a posteriori likelihood vs. median of the posteriors).

⁷ A redshift of $z = 8.38$ was previously adopted for A2744-YD4 by Laporte et al. (2017), but recent *JWST*/NIRSpec observations from Morishita et al. (2022) indicate the source is likely to be at $z = 7.88$ instead.

across the three sources. The unconstrained dust temperature for REBELS-12 results in a relatively large tail towards higher T_{dust} in the stacked posterior distribution. However, the combination of a low global [O III]/[C II] ratio and a Band 8 non-detection may imply that REBELS-12, too, hosts relatively cold dust (see also Section 6.4).

For the $z \gtrsim 5.5$ literature sample, we determine a median dust temperature of $\langle T_{\text{dust},z} \rangle = 45^{+86}_{-14}$ K by concatenating the posteriors obtained from fitting our fiducial MBB model. The long tail of this distribution towards high temperatures is the result of the stringent continuum non-detection at $158 \mu\text{m}$ for both lensed galaxies at $z \sim 8$, MACS0416-Y1 and A2744-YD4. Upon leaving out these sources, we determine a median dust temperature of $\langle T_{\text{dust},z} \rangle = 41^{+56}_{-12}$ K, still slightly higher than the median temperature determined for the three REBELS sources presented in this work. This could be due to the low-S/N detections for part of the comparison sample, or due to an intrinsically higher dust temperature. In the latter case, Band 8 observations do not probe the peak of the dust emission, such that the temperature cannot accurately be constrained even in the case of a high-S/N detection. This, too, manifests as a long tail of plausible high-temperature solutions in the T_{dust} posterior distribution (see also Bakx et al. 2020), at least as long as one adopts a sufficiently conservative prior on the dust temperature to allow for such hot dust.

We proceed by comparing to various redshift-dependent parameterizations of the dust temperature, obtained from stacking either observed (Schreiber et al. 2018; Viero et al. 2022) or simulated (Liang et al. 2019; Schneider et al. in prep) galaxy samples, and the physical model from Sommovigo et al. (2022a).

Through stacking UV-selected galaxies in *Herschel* maps, Schreiber et al. (2018) obtain a linear trend between T_{dust} and redshift ranging from 20 K locally to 40 K at $z \sim 4$ (see also Béthermin et al. 2015). However, several recent studies have shown widely contrasting results in terms of dust temperature evolution. For instance, Drew & Casey (2022) find no evidence for an increase in T_{dust} out to $z \approx 2$, while, in contrast, Viero et al. (2022) prefer a rapidly rising dust temperature that reaches a typical $T_{\text{dust}} \sim 100$ K at $z \approx 8$. The high temperatures measured by the latter are consistent with the two $z \sim 8$ lensed galaxies observed by Laporte et al. (2017) and Bakx et al. (2020), but appear inconsistent with the majority of the known $z \gtrsim 6$ population, including our REBELS targets. As Viero et al. (2022) admit, the high-redshift sample they use for stacking is likely to show significant contamination from low-redshift interlopers, thereby potentially biasing the temperature upwards (see also the discussion in Sommovigo et al. 2022b).

Instead, better agreement is found with the trends from Liang et al. (2019), Sommovigo et al. (2022a) and the dustyGadget simulations (Graziani et al. 2020; Di Cesare et al. 2023, Schneider et al. in prep), which all predict a slightly increasing dust temperature towards higher redshift. Liang et al. (2019) focus on the dust temperatures of ~ 30 galaxies identified in the MassiveFIRE cosmological zoom-in simulations (Feldmann et al. 2016), with stellar masses spanning $10^9 \leq M_{\star}/M_{\odot} \leq 10^{11}$ at $z = 6$. They use radiative transfer code SKIRT (Baes et al. 2011) to generate dust SEDs and self-consistently calculate galaxy dust temperatures. While they do not find evidence for a strong correlation between stellar mass and (peak) dust temperature, Liang et al. (2019) find temperatures of $T_{\text{dust}}(z = 6) \approx 35 - 40$ K for $M_{\star} \sim 10^{10} M_{\odot}$ galaxies, in agreement with the values derived for our similarly massive REBELS targets.⁸

⁸ We note that Liang et al. (2019) fit a trend to the peak dust temperature, $T_{\text{dust}}^{\text{peak}} \propto \lambda_{\text{peak}}^{-1}$, where λ_{peak} is the wavelength where the dust SED peaks. How-

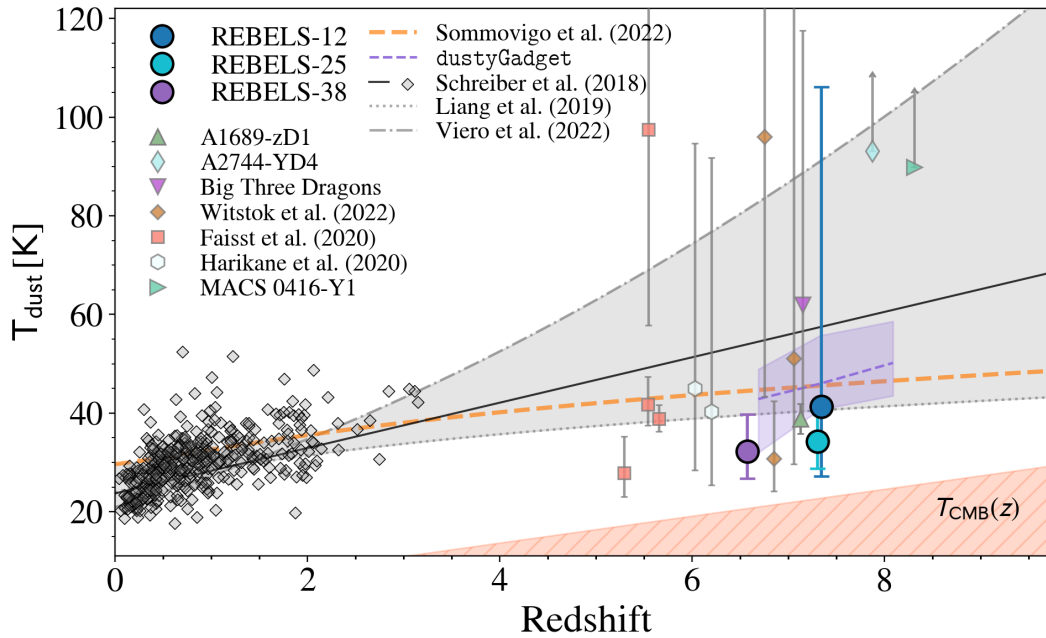


Figure 8. Dust temperature as a function of redshift for the three REBELS targets analyzed in this work (large circles). In addition, we consistently analyze all sources at $z > 5$ with multi-frequency ALMA continuum observations, at least one of which constitutes a detection, using $\beta = 2.0$. At $z \lesssim 4$, we show the individual galaxies from Schreiber et al. (2018). We additionally include their linear fit as the solid black line. Moreover, we overplot the $T_{\text{dust}} - z$ relations from Liang et al. (2019), Sommovigo et al. (2022a), Viero et al. (2022) and dustyGadget (Schneider et al. in prep) as indicated in the legend. The grey shading highlights the large spread in these relations, which extend up to $T_{\text{dust}} \sim 100$ K at $z \sim 7$. In contrast, REBELS-25 and REBELS-38 are both among the coldest known sources at this redshift.

In addition, by considering the dust temperatures of their full sample between $2 \lesssim z \lesssim 6$, Liang et al. (2019) fit a trend between T_{dust} and redshift to all galaxies in their sample with $L_{\text{IR}} > 10^{11} L_{\odot}$, which predicts $T_{\text{dust}}(z = 7) \approx 40$ K, consistent with our measurements.

In addition, our results are in reasonable agreement with the models from Sommovigo et al. (2022a). They argue that the dust temperatures of massive, relatively metal-rich galaxies depend predominantly on their depletion timescales, whereby sources with a shorter t_{depl} are expected to be hotter. Using the redshift-dependent parameterization of the depletion timescale from Tacconi et al. (2020), their models predict a typical $T_{\text{dust}}(z = 7) \approx 45$ K.⁹ While slightly hotter (by ~ 10 K) than the temperatures determined for our Band 8 detected REBELS targets, their model can physically explain the scatter towards lower dust temperatures by supposing colder galaxies have longer depletion timescales (see also Section 6.4).

Finally, we compare our results to the dust temperatures computed at $6.7 \lesssim z \lesssim 8.1$ from the dustyGadget simulations (Schneider et al. in prep), obtained from post-processing the simulations with SKIRT. Galaxy-averaged dust temperatures are computed by modelling the absorption and re-emission of individual dust patches within the galaxy, assuming each emits as a modified blackbody. In Figure 8, we show the typical peak dust temperature obtained from averaging

the temperatures across the simulated galaxy sample at three distinct redshifts. The temperatures obtained from dustyGadget show a slight redshift dependence, and predict a typical temperature of $T_{\text{dust}} \sim 40 - 45$ K at $z \approx 7$, in good agreement with the measurements for REBELS-25 and REBELS-38.

In summary, the dust temperatures we measure for our REBELS sample are among the lowest observed thus far at $z \approx 7$. However, the temperatures are in agreement with those predicted from simulations (Liang et al. 2019, Schneider et al. in prep), and the physical model from Sommovigo et al. (2022a). This may indicate that galaxies with $T_{\text{dust}} \gg 50$ K are outliers at $z \gtrsim 6$, and that typical dust temperatures exhibit only a moderate increase towards high redshift.

6.3 The Dust Properties of UV-Bright Galaxies at $z = 7$

We proceed by discussing the dust properties of the three REBELS targets analyzed in this work. As before, we adopt the analysis using an optically thin modified blackbody with a fixed $\beta = 2.0$ as our fiducial model. We convert the measured IR luminosities to dust-obscured star formation rates via $\text{SFR}_{\text{IR}}/(M_{\odot} \text{ yr}^{-1}) = 1.2 \times 10^{-10} \times (L_{\text{IR}}/L_{\odot})$ (Bouwens et al. 2022). For REBELS-25 and REBELS-38, which are continuum-detected at both rest-frame $90 \mu\text{m}$ and $160 \mu\text{m}$, we determine obscured SFRs of $64^{+39}_{-22} M_{\odot} \text{ yr}^{-1}$ and $28^{+19}_{-9} M_{\odot} \text{ yr}^{-1}$, respectively. These values indicate that the bulk of the star formation in these galaxies is obscured, with $f_{\text{obs}} = \text{SFR}_{\text{IR}}/(\text{SFR}_{\text{IR}} + \text{SFR}_{\text{UV}}) = 0.82^{+0.07}_{-0.08}$ and $0.62^{+0.12}_{-0.11}$ for REBELS-25 and REBELS-38, respectively. Despite our finding that these sources have a lower infrared luminosity than previously expected based on a Band 6 detection and the Sommovigo et al. (2022a)

ever, for our fiducial model of optically thin dust with $\beta = 2.0$, the modified blackbody temperature and peak temperature are equal to one another.

⁹ When instead assuming the depletion timescale traces the cosmic halo accretion rate as predicted by numerical simulations, Sommovigo et al. (2022a) estimate a higher temperature of $T_{\text{dust}}(z = 7) \approx 55$ K.

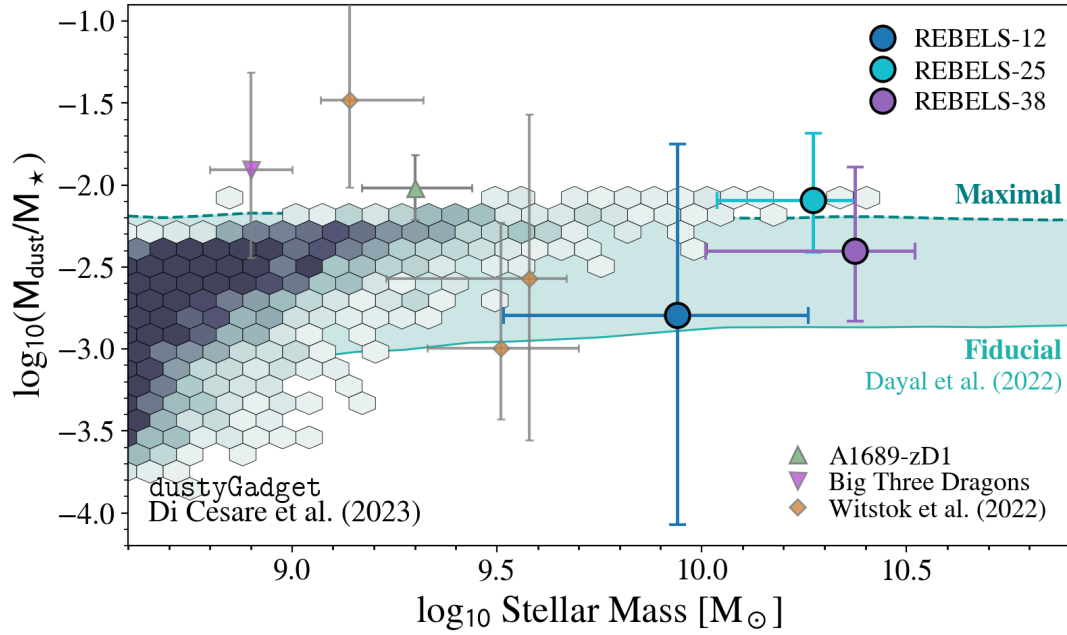


Figure 9. A comparison of the inferred dust masses for our REBELS targets, expressed as the ratio of dust-to-stellar mass, with observations and simulations of high-redshift galaxies. We show a compilation of $z \approx 7$ sources with robust temperature measurements, as well as the models from Dayal et al. (2022) and Di Cesare et al. (2023). For the latter, we represent bins of simulated galaxies with hexagons, with darker bins including a larger number of sources. The dust masses inferred for REBELS agree with the massive end of the simulated sample from dustyGadget at $z = 6.7$, which predict $\log_{10}(M_{\text{dust}}/M_{\star}) \approx -2$. In addition, our findings agree with the models from Dayal et al. (2022), though REBELS-25 would require rapid dust build-up and little destruction as in their “maximal” model. Overall, we conclude that while high, the dust masses observed in our massive $z \sim 7$ sample can be reproduced by current state-of-the-art models and simulations.

models, their obscured fraction remains larger than that of the average REBELS sample based on Band 6 observations alone ($\langle f_{\text{obs}} \rangle \approx 0.45$; Algera et al. 2023), reinforcing the highly obscured nature of these luminous UV-selected sources.

The inferred dust masses for REBELS-25 and REBELS-38 are similarly significant. REBELS-25, in particular, has an inferred dust mass of $\log_{10}(M_{\text{dust}}/M_{\odot}) = 8.13^{+0.37}_{-0.26}$ given $\beta = 2.0$. Making use of the stellar masses determined by Topping et al. (2022), we find its dust-to-stellar mass ratio to be $M_{\text{dust}}/M_{\star} = 8.1^{+12.6}_{-4.2} \times 10^{-3}$. For REBELS-38, we infer a slightly lower dust mass of $\log_{10}(M_{\text{dust}}/M_{\odot}) = 7.90^{+0.39}_{-0.35}$, and similarly a slightly lower $M_{\text{dust}}/M_{\star} = 4.0^{+8.9}_{-2.5} \times 10^{-3}$.

We show these dust-to-stellar mass ratios in the context of models of dust production and destruction in Figure 9. In addition, we overplot five sources (three from Witstok et al. 2022, A1689-zD1 and the Big Three Dragons) for which stellar mass measurements are available in the literature, and which provided robust temperature measurements in Section 6.2. We note that the literature stellar masses are based on parametric SED fitting, and may therefore be underestimated. For REBELS, for example, non-parametric mass measurements are larger than those obtained for an assumed constant SFH by a typical ~ 0.4 dex (Topping et al. 2022).

Utilizing the dust masses estimated from the single-band REBELS observations at rest-frame $158 \mu\text{m}$, Dayal et al. (2022) investigate the dust build-up of the REBELS sample through the Delphi semi-analytical model. Their fiducial model, which predicts a typical $M_{\text{dust}}/M_{\star} \sim 10^{-3}$, can readily explain the dust contents for 11/13 of the dust- and [C II]-detected REBELS galaxies, which they predict is predominantly due to dust produced in supernovae. For the remain-

ing two sources – the low-mass REBELS-19 and REBELS-39 – they require minimal dust destruction/ejection, and rapid grain growth in the ISM (the “maximal dust” model in Dayal et al. 2022, which predicts $M_{\text{dust}}/M_{\star} \sim 6 - 7 \times 10^{-3}$). For REBELS-25 and REBELS-38, we now infer $\sim 0.4 - 0.5$ dex larger dust masses compared to the earlier estimates based on the [C II] and underlying continuum emission in these sources from Sommovigo et al. (2022a).¹⁰ REBELS-38 now falls between the fiducial and maximal dust models, while REBELS-25 requires dust build-up nearly as rapid as in the maximal dust model.

We next compare the measured dust masses for REBELS with those found across a large sample of $z = 6.7$ galaxies in the dustyGadget simulations by Di Cesare et al. (2023). Their hydrodynamical simulations include a two-phase ISM, which facilitates the modelling of various dust production and destruction mechanisms based on the local physical conditions in the galaxy. In particular, dust is produced through a combination of supernovae, AGB stars and grain growth in the ISM, while it may be destroyed in a variety of processes such as shocks, astration and sputtering (Graziani et al. 2020; Di Cesare et al. 2023). The dustyGadget simulations are capable of producing large dust reservoirs in massive ($M_{\star} \gtrsim 10^{10} M_{\odot}$) galaxies already at $z \approx 7$, reaching up to $M_{\text{dust}}/M_{\star} \sim 10^{-2}$. As such, their models are in excellent agreement with the inferred dust properties of our REBELS targets.

Overall, we conclude that REBELS-25 and REBELS-38 have mas-

¹⁰ For consistency, we adopt the dust masses predicted by Sommovigo et al. (2022a) adapted to the stellar masses from Topping et al. (2022) used in this work; these are provided in Sommovigo et al. (2022b).

sive dust reservoirs of $M_{\text{dust}} \sim 10^8 M_{\odot}$, corresponding to a significant fraction of their stellar mass ($\sim 0.4\text{--}0.8\%$). Nevertheless, the inferred dust masses are consistent with those predicted by state-of-the-art models of dust production in the early Universe, and demonstrate that dust build-up can proceed in a rapid manner at high redshift. In the future, larger samples of massive, dusty galaxies will allow for a detailed investigation of the relative contributions of the various avenues of dust production in the earliest galaxies.

6.4 An Evolved Star-forming Population at Redshift 7

In the previous sections, we have outlined how our REBELS targets are characterized by 1) low [O III]/[C II] ratios, and 2) low dust temperatures compared to the known $z \geq 6$ population. In addition, our targets have relatively high dust masses ($M_{\text{dust}} \sim 10^8 M_{\odot}$) as well as high stellar masses ($M_{\star} \sim 10^{10} M_{\odot}$). All of these characteristics indicate that the three REBELS sources analyzed in this work have previously experienced one (or multiple) burst(s) of star formation, while currently residing in a less bursty state. Indeed, while their inferred burstiness parameters ($\kappa_s \sim 15\text{--}20$; Section 6.1) place these galaxies ~ 1 dex above the *local* Schmidt-Kennicutt relation, they appear less bursty than the previously observed $z \geq 6$ population.

As an independent tracer of burstiness, we consider the combined equivalent width (EW) of the [O III] $\lambda\lambda 4959, 5007$ doublet and H β line [denoted EW([O III] + H β)], which are redshifted into the *Spitzer*/IRAC channels for galaxies at $z \geq 6.5$ and are capable of significantly contributing to the observed broadband fluxes (e.g., Smit et al. 2014, 2015; Roberts-Borsani et al. 2016; Schouws et al. 2022a). Given that these are nebular emission lines, they trace the recent formation of massive stars, and hence form a proxy for galaxy burstiness.

By fitting non-parametric SFHs to available rest-UV/optical observations of the REBELS sample, Topping et al. (2022) find a mean equivalent width of EW([O III] + H β) = 735^{+97}_{-93} Å at $z \sim 7$, in agreement with previous results from Endsley et al. (2021). REBELS-25 and REBELS-38, however, have an inferred EW([O III] + H β) = 127^{+327}_{-92} Å and 143^{+617}_{-91} Å, significantly below the REBELS average, while REBELS-12, on the other hand, is characterized by an equivalent width of EW([O III] + H β) = 2217^{+710}_{-981} Å, among the largest in REBELS.

The low expected burstiness of REBELS-25 and REBELS-38 is therefore supported by their relatively small [O III] + H β equivalent widths, while the EW of REBELS-12 implies significant bursty star formation, in apparent contrast with its observed [O III]/[C II] line ratio. It is possible that the complex kinematics inferred from its broad [C II] line lie at the basis of this discrepancy in REBELS-12. As discussed in Section 5.2.1, this source may be an ongoing merger, whereby the [O III] $88 \mu\text{m}$ emitting system dominates the EW([O III] + H β). The measured line ratio of this component, [O III]/[C II] = $3.3^{+3.3}_{-1.0}$, would bring the system into closer agreement with the line ratios of [O III]/[C II] $\sim 2\text{--}8$ inferred for the five $z \sim 7$ galaxies from Wistok et al. (2022), which are also characterized by a relatively high EW([O III] + H β) $\approx 600\text{--}1400$ Å. We further note that, while the non-detection of REBELS-12 at rest-frame $90 \mu\text{m}$ likely implies a low dust temperature, we cannot currently rule out warmer dust, which in turn might be indicative of a larger burstiness.

In what follows, we therefore focus on REBELS-25 and REBELS-38. We can interpret their lack of bursty star formation as both sources having a long depletion timescale ($t_{\text{depl}} = M_{\text{gas}}/\text{SFR}$), for which we can provide a rough estimate by converting their [C II] luminosities into a molecular gas mass following Zanella et al. (2018), resulting

in $\log_{10}(M_{\text{gas}}/M_{\odot}) = 10.7 \pm 0.3$ for both targets. We note, however, that the conversion from [C II] luminosity to molecular gas masses is inherently quite uncertain, and may depend on the physical properties and conditions of the galaxy (e.g., Israel 2020; Vizgan et al. 2022). As such, we refer to Aravena et al. (submitted) for a more detailed discussion of [C II]-based molecular gas masses.

Utilizing the total (UV + IR) SFRs, we determine a depletion timescale of $t_{\text{depl}} = 620^{+750}_{-340}$ Myr and $t_{\text{depl}} = 1090^{+1310}_{-590}$ Myr for REBELS-25 and REBELS-38, respectively. While the uncertainties are large, these depletion timescales appear higher than the typical depletion time found for the ALPINE sample at $z \sim 5.5$ by Dessauges-Zavadsky et al. (2020) of $t_{\text{depl}} = 230\text{--}460$ Myr. In addition, the estimated depletion times exceed an extrapolation of the redshift-dependent trend from Tacconi et al. (2018), which predicts $t_{\text{depl}} \sim 300$ Myr at $z = 7$. As such, REBELS-25 and REBELS-38 may indeed show longer depletion timescales than expected for the typical galaxy population at this epoch.

In other words, compared to the known $z \geq 6$ population, our targets may have higher gas masses given their SFRs, and therefore also larger dust masses, assuming a simple (metallicity-dependent) scaling between dust and gas mass known as the dust-to-gas ratio (e.g., Rémy-Ruyer et al. 2014). This is indeed corroborated by our observations, which indicate large dust masses of $M_{\text{dust}} \sim 10^8 M_{\odot}$ for REBELS-25 and REBELS-38. Such elevated dust masses could then provide a natural explanation for the low observed temperatures, as a larger dust content implies there is, on average, less energy available per unit dust mass to heat the dust to higher temperatures.

We caveat, however, that the spatial distribution of dust within the galaxy is expected to additionally affect the measured dust temperatures. For example, if dust is preferentially located directly around sites of star formation, a higher dust temperature would be inferred observationally given that a hot dust component can dominate the infrared luminosity of a galaxy even if it contributes little to the overall dust mass (e.g., Liang et al. 2019). A low dust temperature, on the other hand, could therefore also be the result of spatial segregation between the sites of star formation and the dust. We emphasize that high-resolution dust continuum observations are required to test this scenario in detail. However, given the constraints on the burstiness of our sources from the [O III]/[C II] ratio, long depletion timescales and low EW([O III] + H β), our preferred interpretation is a scenario where the low dust temperatures are the result of a lack of bursty star formation resulting in the inefficient heating of a massive dust reservoir.

7 SUMMARY

We present new ALMA Band 8 ($\lambda_{\text{rest}} \approx 90 \mu\text{m}$) observations of three massive UV-selected galaxies ($M_{\star} \approx 10^{9.9\text{--}10.4} M_{\odot}$) at $z \sim 7$, REBELS-12, REBELS-25 and REBELS-38, in order to constrain their far-infrared spectral energy distributions. All three targets were previously detected in [C II] $158 \mu\text{m}$ emission and underlying Band 6 continuum (Schouws et al. in prep and Inami et al. 2022, respectively). The new Band 8 observations additionally target the [O III] $88 \mu\text{m}$ line in REBELS-12 and REBELS-25, allowing insight into their global ISM properties through the [O III]/[C II] line ratio. Our main conclusions are as follows:

- We detect Band 8 continuum emission in REBELS-25 (4.4σ) and REBELS-38 (5.3σ), and determine an upper limit for REBELS-12 ($< 3\sigma$). REBELS-38 is marginally spatially resolved in the continuum map and shows a two-component dust morphology which was not previously visible in the lower resolution Band 6 observations.

Using the (tapered) dual-band ALMA data, we measure dust temperatures for our sample through modified blackbody fitting. Adopting a fiducial model of an optically thin MBB with $\beta = 2.0$, we measure relatively cold dust temperatures for REBELS-25 and REBELS-38 of $T_{\text{dust}} \sim 30 - 35$ K, while the dust temperature of REBELS-12 cannot be accurately constrained.

- We compare the dust temperatures of our targets to literature sources at $z \gtrsim 5$ by fitting them in a consistent manner, and find that the REBELS galaxies are among the coldest known sources at this epoch. Nevertheless, the measured temperatures are in good agreement with those predicted by simulations (e.g., [Liang et al. 2019](#); [Schneider et al. in prep](#)) and with the models from [Sommovigo et al. \(2022a\)](#), while being significantly lower than (extrapolations of) stacked samples at $z \sim 7$ ([Schreiber et al. 2018](#); [Viero et al. 2022](#)).

- Given that REBELS-25 and REBELS-38 have low inferred dust temperatures, yet are robustly detected in both ALMA Bands 6 and 8, they require large dust masses of $M_{\text{dust}} \sim 10^8 M_{\odot}$. Their dust-to-stellar mass ratios are $\sim 0.4 - 0.8\%$, which necessitate rapid dust build-up. However, the dust contents of REBELS-25 and REBELS-38 are consistent with those predicted for massive galaxies by simulations ([Dayal et al. 2022](#); [Di Cesare et al. 2023](#)).

- We detect [O III]88 μm emission in both REBELS-12 and REBELS-25, and find $[\text{O III}]/[\text{C II}] \approx 1 - 1.5$, lower by a factor of $2 - 8\times$ compared to the previously observed population of $6 \lesssim z \lesssim 9$ galaxies. However, we note that the [C II] line profile of REBELS-12 is significantly broader than its [O III] emission, suggesting it may be a merger of an [O III]-bright and [O III]-dark component with individual line ratios of $[\text{O III}]/[\text{C II}] = 3.3^{+3.3}_{-1.0}$ and $[\text{O III}]/[\text{C II}] < 1.1$. Higher resolution ALMA data are required to investigate this scenario in further detail.

- Through the models of [Vallini et al. \(2021\)](#), we link the [O III]/[C II] ratios to the physical properties of our targets. In particular, the low line ratios indicate that our targets are likely to be less bursty than the known $z \gtrsim 6$ galaxy population. Instead, the three REBELS sources are likely characterized by weaker ionizing radiation fields due to their lower star formation rate surface densities. This interpretation is consistent with the low EW([O III] + H β) ≈ 140 Å inferred from broadband *Spitzer*/IRAC fluxes for REBELS-25 and REBELS-38 ([Topping et al. 2022](#)).

The REBELS sources analyzed in this work are thus characterized by low dust temperatures, high dust and stellar masses and low [O III]/[C II] ratios. Taken together, this implies that they may be relatively evolved star-forming galaxies already at $z \approx 7$. The low emission line ratios likely indicate that our targets are currently steadily forming stars, as opposed to in a bursty manner, translating into longer depletion timescales and a low heating efficiency per unit dust mass, resulting in lower overall dust temperatures.

Further dual/multi-band ALMA observations targeting a larger number of $z \sim 7$ galaxies are required to elucidate whether this relatively evolved evolutionary state may indeed be common in high-redshift sources, or whether the galaxies analyzed in this work constitute a less common yet highly interesting population at this epoch.

ACKNOWLEDGEMENTS

This paper made use of the following software packages: spectral-cube ([Ginsburg et al. 2019](#)), radio-beam ([Koch et al. 2021](#)), interferopy ([Boogaard et al. 2021](#)) and GLAM ([Vallini et al. 2021](#)).

The authors thank the referee for providing useful feedback that improved the quality of this manuscript. The authors also thank Livia

Vallini for help with the GLAM software package, Monica Relaño for providing feedback on the draft and Claudia di Cesare for sharing data from the dustyGadget simulations.

This work was supported by NAOJ ALMA Scientific Research Grant Code 2021-19A (HSBA and HI). PD acknowledges support from the NWO grant 016.VIDI.189.162 (“ODIN”) and from the European Commission’s and University of Groningen’s CO-FUND Rosalind Franklin program. MA acknowledges support from FONDECYT grant 1211951 and ANID BASAL project FB210003. IDL and MP acknowledge support from ERC starting grant 851622 DustOrigin. RS acknowledges support from a STFC Ernest Rutherford Fellowship (ST/S004831/1). MS acknowledges support from the CIDEAGENT/2021/059 grant, from project PID2019-109592GB-I00/AEI/10.13039/501100011033 from the Spanish Ministerio de Ciencia e Innovación - Agencia Estatal de Investigación, and from Proyecto ASFAE/2022/025 del Ministerio de Ciencia y Innovación en el marco del Plan de Recuperación, Transformación y Resiliencia del Gobierno de España.

DATA AVAILABILITY

The data underlying this article will be made available upon reasonable request to the corresponding author.

REFERENCES

- Akins H. B., et al., 2022, *ApJ*, **934**, 64
 Algera H. S. B., et al., 2023, *MNRAS*, **518**, 6142
 Arata S., Yajima H., Nagamine K., Abe M., Khochfar S., 2020, *MNRAS*, **498**, 5541
 Atek H., et al., 2022, arXiv e-prints, p. arXiv:2207.12338
 Baes M., Verstaappen J., De Looze I., Fritz J., Saftly W., Vidal Pérez E., Stalewski M., Valcke S., 2011, *ApJS*, **196**, 22
 Bakx T. J. L. C., et al., 2020, *MNRAS*, **493**, 4294
 Bakx T. J. L. C., et al., 2021, *MNRAS*, **508**, L58
 Barrufet L., et al., 2023, *MNRAS*, **522**, 3926
 Behrens C., Pallottini A., Ferrara A., Gallerani S., Vallini L., 2018, *MNRAS*, **477**, 552
 Béthermin M., et al., 2015, *A&A*, **573**, A113
 Bianchi S., 2013, *A&A*, **552**, A89
 Blain A. W., Smail I., Ivison R. J., Kneib J. P., Frayer D. T., 2002, *Phys. Rep.*, **369**, 111
 Blain A. W., Barnard V. E., Chapman S. C., 2003, *MNRAS*, **338**, 733
 Boogaard L., Meyer R. A., Novak M., 2021, Interferopy: analysing datacubes from radio-to-submm observations, Zenodo, doi:10.5281/zenodo.5775604
 Bouwens R. J., et al., 2015, *ApJ*, **803**, 34
 Bouwens R. J., et al., 2022, *ApJ*, **931**, 160
 Bowler R. A. A., Bourne N., Dunlop J. S., McLure R. J., McLeod D. J., 2018, *MNRAS*, **481**, 1631
 Calzetti D., Armus L., Bohlin R. C., Kinney A. L., Koornneef J., Storchi-Bergmann T., 2000, *ApJ*, **533**, 682
 Carniani S., et al., 2017, *A&A*, **605**, A42
 Carniani S., et al., 2020, *MNRAS*, **499**, 5136
 Casey C. M., 2012, *MNRAS*, **425**, 3094
 Casey C. M., Narayanan D., Cooray A., 2014, *Phys. Rep.*, **541**, 45
 Casey C. M., et al., 2019, *ApJ*, **887**, 55
 Castellano M., et al., 2022, arXiv e-prints, p. arXiv:2207.09436
 Chabrier G., 2003, *PASP*, **115**, 763
 Conley A., et al., 2011, *ApJ*, **732**, L35
 Cormier D., et al., 2012, *A&A*, **548**, A20
 Cormier D., et al., 2019, *A&A*, **626**, A23
 Cortzen I., et al., 2020, *A&A*, **634**, L14
 Da Cunha E., et al., 2013, *ApJ*, **766**, 13

- Da Cunha E., et al., 2021, *ApJ*, 191, 30
- Dayal P., et al., 2022, *MNRAS*, 512, 989
- De Looze I., et al., 2014, *A&A*, 568, A62
- Dessauges-Zavadsky M., et al., 2020, *A&A*, 643, A5
- Di Cesare C., Graziani L., Schneider R., Ginolfi M., Venditti A., Santini P., Hunt L. K., 2023, *MNRAS*, 519, 4632
- Díaz-Santos T., et al., 2017, *ApJ*, 846, 32
- Draine B. T., 1989, in Böhm-Vitense E., ed., *Infrared Spectroscopy in Astronomy*, p. 93
- Draine B. T., 2003, *ARA&A*, 41, 241
- Drew P. M., Casey C. M., 2022, *ApJ*, 930, 142
- Dudzevičiūtė U., et al., 2020, *MNRAS*, 494, 3828
- Endsley R., Stark D. P., Chevillard J., Charlot S., 2021, *MNRAS*, 500, 5229
- Faisst A. L., et al., 2020, *ApJS*, 247, 61
- Feldmann R., Hopkins P. F., Quataert E., Faucher-Giguère C.-A., Kereš D., 2016, *MNRAS*, 458, L14
- Ferland G. J., Korista K. T., Verner D. A., Ferguson J. W., Kingdon J. B., Verner E. M., 1998, *PASP*, 110, 761
- Ferland G. J., et al., 2017, *Rev. Mex. Astron. Astrofis.*, 53, 385
- Ferrara A., Vallini L., Pallottini A., Gallerani S., Carniani S., Kohandel M., Decataldo D., Behrens C., 2019, *MNRAS*, 489, 1
- Ferrara A., et al., 2022, *MNRAS*, 512, 58
- Finkelstein S. L., et al., 2015, *ApJ*, 810, 71
- Foreman-Mackey D., Hogg D. W., Lang D., Goodman J., 2013, *PASP*, 125, 306
- Fudamoto Y., et al., 2021, *Nature*, 597, 489
- Fudamoto Y., Inoue A. K., Sugahara Y., 2022a, arXiv e-prints, p. arXiv:2206.01879
- Fudamoto Y., et al., 2022b, *ApJ*, 934, 144
- Fujimoto S., et al., 2020, *ApJ*, 900, 1
- Ginsburg A., et al., 2019, radio-astro-tools/spectral-cube: Release v0.4.5, Zenodo, doi:10.5281/zenodo.3558614
- Glatzle M., Ciardi B., Graziani L., 2019, *MNRAS*, 482, 321
- Gould R. J., Salpeter E. E., 1963, *ApJ*, 138, 393
- Graziani L., Schneider R., Ginolfi M., Hunt L. K., Maio U., Glatzle M., Ciardi B., 2020, *MNRAS*, 494, 1071
- Greve T. R., et al., 2012, *ApJ*, 756, 101
- Gullberg B., et al., 2015, *MNRAS*, 449, 2883
- Harikane Y., et al., 2020, *ApJ*, 896, 93
- Harikane Y., et al., 2022, arXiv e-prints, p. arXiv:2208.01612
- Hashimoto T., et al., 2018, *Nature*, 557, 392
- Hashimoto T., et al., 2019, *PASJ*, 71, 71
- Hayes M., Schaefer D., Östlin G., Mas-Hesse J. M., Atek H., Kunth D., 2014, *ApJ*, 730, 8
- Hildebrand R. H., 1983, *QJRAS*, 24, 267
- Hirashita H., Ferrara A., 2002, *MNRAS*, 337, 921
- Hodge J. A., da Cunha E., 2020, *Royal Society Open Science*, 7, 200556
- Hogg D. W., Foreman-Mackey D., 2018, *ApJS*, 236, 11
- Hygate et al. A., 2022, *MNRAS*, submitted
- Inami H., et al., 2022, *MNRAS*, 515, 3126
- Inoue A. K., et al., 2016, *Science*, 352, 1559
- Inoue A. K., Hashimoto T., Chihara H., Koike C., 2020, *MNRAS*, 495, 1577
- Israel F. P., 2020, *A&A*, 635, A131
- Jarvis M. J., et al., 2013, *MNRAS*, 428, 1281
- Jin S., et al., 2022, *A&A*, 665, A3
- Johnson B. D., Leja J., Conroy C., Speagle J. S., 2021, *ApJS*, 254, 22
- Jones G. C., Maiolino R., Caselli P., Carniani S., 2020, *MNRAS*, 498, 4109
- Katz H., Kimm T., Sijacki D., Haehnelt M. G., 2017, *MNRAS*, 468, 4831
- Katz H., et al., 2022, *MNRAS*, 510, 5603
- Kennicutt R. C., Evans N. J., 2012, *ARA&A*, 50, 531
- Koch E., et al., 2021, radio-astro-tools/radio-beam: v0.3.3, Zenodo, doi:10.5281/zenodo.4623788
- Kohandel M., Pallottini A., Ferrara A., Zanella A., Behrens C., Carniani S., Gallerani S., Vallini L., 2019, *MNRAS*, 487, 3007
- Lagache G., Cousin M., Chatzikos M., 2018, *A&A*, 609, A130
- Laporte N., et al., 2017, *ApJ*, 837, L21
- Laporte N., et al., 2019, *MNRAS*, 487, L81
- Leja J., Carnall A. C., Johnson B. D., Conroy C., Speagle J. S., 2019, *ApJ*, 876, 3
- Leja J., Speagle J. S., Johnson B. D., Conroy C., van Dokkum P., Franx M., 2020, *ApJ*, 893, 111
- Liang L., et al., 2019, *MNRAS*, 489, 1397
- Lupi A., Bovino S., 2020, *MNRAS*, 492, 2818
- Lutz D., et al., 2016, *A&A*, 591, A136
- Ma X., et al., 2018, *MNRAS*, 478, 1694
- Mancini M., Schneider R., Graziani L., Valiante R., Dayal P., Maio U., Ciardi B., Hunt L. K., 2015, *MNRAS*, 451, L70
- McCracken H. J., et al., 2012, *A&A*, 544, A156
- McLure R. J., et al., 2013, *MNRAS*, 432, 2696
- Michałowski M. J., 2015, *A&A*, 577, A80
- Mohan N., Rafferty D., 2015, PyBDSF: Python Blob Detection and Source Finder, Astrophysics Source Code Library (ascl:1502.007)
- Morishita T., et al., 2022, arXiv e-prints, p. arXiv:2211.09097
- Naidu R. P., et al., 2022, arXiv e-prints, p. arXiv:2207.09434
- Oesch P. A., Bouwens R. J., Illingworth G. D., Labbé I., Stefanon M., 2018, *ApJ*, 855, 105
- Ono Y., et al., 2022, *ApJ*, 941, 74
- Pallottini A., et al., 2022, *MNRAS*, 513, 5621
- Popping G., Somerville R. S., Galametz M., 2017, *MNRAS*, 471, 3152
- Rémy-Ruyer A., et al., 2014, *A&A*, 563, A31
- Roberts-Borsani G. W., et al., 2016, *ApJ*, 823, 143
- Sawicki M., 2012, *PASP*, 124, 1208
- Schaefer D., et al., 2020, *A&A*, 643, A3
- Schouws S., et al., 2022a, arXiv e-prints, p. arXiv:2202.04080
- Schouws S., et al., 2022b, *ApJ*, 928, 31
- Schreiber C., Elbaz D., Pannella M., Ciesla L., Wang T., Franco M., 2018, *A&A*, 609, A30
- Scoville N., et al., 2007, *ApJS*, 172, 1
- Simpson J. M., et al., 2017, *ApJ*, 839, 58
- Smit R., et al., 2014, *ApJ*, 784, 58
- Smit R., et al., 2015, *ApJ*, 801, 122
- Sommovigo L., Ferrara A., Pallottini A., Carniani S., Gallerani S., Decataldo D., 2020, *MNRAS*, 497, 956
- Sommovigo L., Ferrara A., Carniani S., Zanella A., Pallottini A., Gallerani S., Vallini L., 2021, *MNRAS*, 503, 4878
- Sommovigo L., et al., 2022a, *MNRAS*, 513, 3122
- Sommovigo L., et al., 2022b, *MNRAS*, 517, 5930
- Stacey G. J., Hailey-Dunsheath S., Ferkinhoff C., Nikola T., Parshley S. C., Benford D. J., Staguhn J. G., Fiolet N., 2010, *ApJ*, 724, 957
- Stark D. P., 2016, *ARA&A*, 54, 761
- Stefanon M., et al., 2019, *ApJ*, 883, 99
- Sugahara Y., et al., 2021, *ApJ*, 923, 5
- Sugahara Y., Inoue A. K., Fudamoto Y., Hashimoto T., Harikane Y., Yamanaka S., 2022, *ApJ*, 935, 119
- Tacconi L. J., et al., 2018, *ApJ*, 853, 179
- Tacconi L. J., Genzel R., Sternberg A., 2020, *ARA&A*, 58, 157
- Tamura Y., et al., 2019, *ApJ*, 874, 27
- Todini P., Ferrara A., 2001, *MNRAS*, 325, 726
- Topping M. W., et al., 2022, *MNRAS*, 516, 975
- Vallini L., Gallerani S., Ferrara A., Pallottini A., Yue B., 2015, *ApJ*, 813, 36
- Vallini L., Ferrara A., Pallottini A., Gallerani S., 2017, *MNRAS*, 467, 1300
- Vallini L., Ferrara A., Pallottini A., Carniani S., Gallerani S., 2021, *MNRAS*, 505, 5543
- Van der Wel A., et al., 2014, *ApJ*, 788, 28
- Viero M. P., Sun G., Chung D. T., Monceli L., Condon S. S., 2022, *MNRAS*, 516, L30
- Vijayan A. P., Clay S. J., Thomas P. A., Yates R. M., Wilkins S. M., Henriques B. M., 2019, *MNRAS*, 489, 4072
- Vijayan A. P., et al., 2022, *MNRAS*, 511, 4999
- Vizgan D., et al., 2022, *ApJ*, 929, 92
- Walter F., et al., 2018, *ApJ*, 869, L22
- Watson D., Christensen L., Knudsen K. K., Richard J., Gallazzi A., Michałowski M. J., 2015, *Nature*, 519, 327
- Weingartner J. C., Draine B. T., 2001, *ApJ*, 548, 296

- Whitler L., Stark D. P., Endsley R., Leja J., Charlot S., Chevallard J., 2022, arXiv e-prints, p. arXiv:2206.05315
- Witstok J., et al., 2022, *MNRAS*, 515, 1751
- Yan H., Ma Z., Ling C., Cheng C., Huang J.-s., Zitrin A., 2022, arXiv e-prints, p. arXiv:2207.11558
- Zanella A., et al., 2018, *MNRAS*, 481, 1976

APPENDIX A: DUST TEMPERATURE POSTERIORS

We show the posterior distributions of the inferred dust temperatures for REBELS-12, REBELS-25 and REBELS-38 in Figure A1, assuming optically thin (top row) and thick dust (bottom row; $\lambda_{\text{thick}} = 100 \mu\text{m}$). For REBELS-12, a long tail towards higher temperatures remains, owing to its non-detection at rest-frame $\sim 90 \mu\text{m}$ and the modest S/N of its Band 6 flux density measurement. The posteriors for REBELS-25 and REBELS-38, on the other hand, are narrow and single-peaked.

APPENDIX B: COMPARISON TO SINGLE-BAND DUST TEMPERATURE MODELLING

In recent years, there has been significant interest in estimating dust temperatures of high-redshift galaxies without having to resort to expensive multi-band ALMA photometry. We here compare our Band 8 dust temperature determinations to two models providing such estimates, described in detail in Sommovigo et al. (2021) and Fudamoto et al. (2022a).

Comparison to Sommovigo et al. (2022a)

Sommovigo et al. (2021) introduce a model to infer dust temperatures and masses through the combined detection of the [C II] emission line and underlying $158 \mu\text{m}$ continuum. In short, their models utilize the fact that both the [C II] and far-infrared luminosities of a galaxy trace its star formation rate, while the [C II] emission is also a proxy for gas mass and therefore by extension dust mass. As a result, a single dust continuum detection combined with an indirect measurement of the infrared luminosity through the [C II]-based SFR provides insight into the dust SED, and hence the dust temperature. A recent application of their models to the $z = 7.13$ lensed galaxy A1689-zD1 by Bakx et al. (2021) demonstrates good agreement between the dust temperature obtained from four-band MBB fitting and the single-band temperature prediction.

In a recent work, Sommovigo et al. (2022a) use their model to estimate the dust temperatures of the thirteen REBELS targets for which both a dust continuum and [C II] detection are available, which includes the three targets analyzed in this work. To be consistent with the Sommovigo et al. (2022a) models, who assume Milky Way-like dust, we compare the dust temperatures obtained when $\beta = 2.0$ is adopted. The results of this comparison are shown in Figure B1 (first two rows). We find that the model predictions overestimate the dust temperatures of REBELS-25 and REBELS-38, for which Band 8 detections are available, by $\Delta T_{\text{dust}} \approx 15 \text{ K}$. For REBELS-12, on the other hand, a comparison of the fitted and predicted dust temperatures provides only limited insight, given the large uncertainty on its MBB-fitted dust temperature.

We can explain the observed difference for REBELS-25 and REBELS-38 by returning to the burstiness parameter κ_s . In their models, Sommovigo et al. (2022a) assumed a uniform distribution for the burstiness for the REBELS sources between $\kappa_s = 1 - 50$,

motivated by the literature sample analyzed in Vallini et al. (2021). Given that the burstiness cannot be constrained with just [C II] information, their inferred posterior on κ_s resembles the prior, which hence corresponds to a typical assumed burstiness of $\kappa_s \sim 25 \pm 15$.

However, using the new [O III] observations for REBELS-12 and REBELS-25, we infer a moderate $\kappa_s \approx 15 - 20$ for our sample (Section 6.1). We therefore re-run the Sommovigo et al. (2022a) models with these lower burstiness parameters, and include the updated dust temperature predictions in Figure B1 (third row). For REBELS-12, we use both the inferred burstiness parameter when considering the full system, and the slightly higher value obtained when considering only the [O III]-bright component. We also re-run the Sommovigo et al. (2022a) models for REBELS-38, for which no [O III] data is available, under the assumption that it has the same burstiness as REBELS-25. Given that REBELS-38, like REBELS-25, is a massive ($M_\star \approx 10^{10.4} M_\odot$; Table 2) galaxy with a low dust temperature, we expect it to similarly have a low [O III]/[C II] ratio.

By assuming these physically motivated lower values for κ_s , the predicted T_{dust} decreases by $\sim 10 \text{ K}$ for REBELS-25 and REBELS-38, thereby improving the agreement with the temperatures inferred through modified blackbody fitting. For REBELS-12, the predicted dust temperature also changes by $\sim 10 \text{ K}$, depending on which burstiness is assumed. However, both values are consistent with the loose constraints obtained from MBB-fitting. Nevertheless, we thus find that care must be taken to adopt suitable priors when adopting single-band dust temperatures.

Comparison to Fudamoto et al. (2022a)

We next compare to the single-band dust temperature model from Fudamoto et al. (2022a), which builds upon the framework by Inoue et al. (2020). In short, their model approximates a galaxy as spherical object of size r_{IR} consisting of uniformly distributed dust clumps within a homogeneous interstellar medium. The galaxy as a whole is assumed to be in radiative equilibrium, which implies that a fraction of the UV emission associated with massive star formation is absorbed by dust and subsequently re-emitted in the infrared regime. Given, then, a measured UV luminosity, infrared size and dust continuum flux density at any single wavelength, a galaxy's dust temperature (and mass) can be inferred under the assumption of a clumpiness parameter (see Inoue et al. 2020 for details). We here assume the average clumpiness parameter of $\log_{10}(\xi) = -1.02 \pm 0.41$ measured across six $z \gtrsim 5$ galaxies with 3 or more ALMA continuum detections by Fudamoto et al. (2022a).

We note that some of the REBELS targets – including REBELS-12 and REBELS-38 analyzed in this work – show evidence for spatial offsets between their dust and UV emission (Inami et al. 2022), which introduces additional uncertainty in the applicability of dust temperature models based upon radiative equilibrium (see also Ferrara et al. 2022). However, in the absence of available high-resolution observations for the bulk of the high-redshift dust-detected population, such models may still provide a useful first-look into their dust properties. As such, we apply the Fudamoto et al. (2022a) models here while keeping this caveat in mind.

We adopt the UV luminosities of our three REBELS targets from Stefanon et al. (in prep), and utilize the IR sizes determined in Section 6.1. For REBELS-12, we investigate two scenarios, whereby we adopt either the total Band 6 flux density across its two dust components, or the flux density in the co-spatial dust component only (Section 6.1). However, we find that the resulting predicted temperatures agree to within $< 2 \text{ K}$. For REBELS-38, we model the

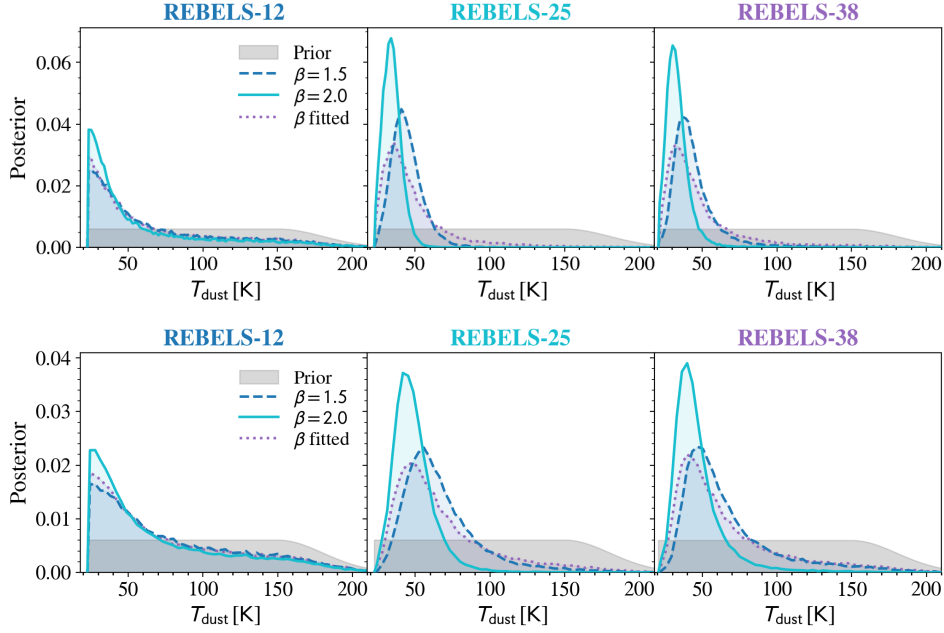


Figure A1. Posterior dust temperature distributions for REBELS-12, REBELS-25 and REBELS-38, assuming optically thin (**top row**) and thick dust ($\lambda_{\text{thick}} = 100 \mu\text{m}$; **bottom row**). The distributions are shown both for a fixed dust emissivity ($\beta = 1.5, 2.0$; dashed and solid lines respectively), as well as for β included in the fit (dotted). The prior on the dust temperature is shown in grey, and is flat for $T_{\text{CMB},z} < T_{\text{dust},z} < 150 \text{ K}$, after which it smoothly decreases by a Gaussian with $\sigma = 30 \text{ K}$. For REBELS-25 and REBELS-38, which have robust detections in both ALMA Bands 6 and 8, the dust temperatures are well constrained, and are independent of the precise shape of the assumed prior.

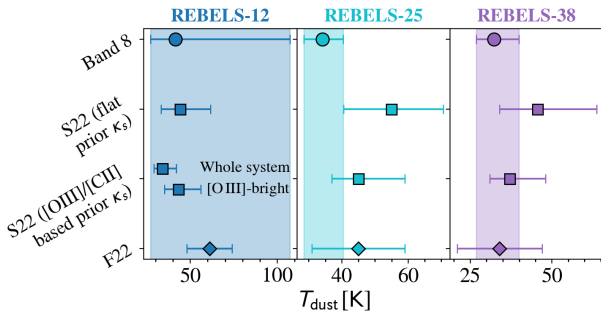


Figure B1. A comparison of different dust temperature measurements for the three REBELS targets discussed in this work. The top row shows T_{dust} obtained from MBB fitting (assuming $\beta = 2.0$), while the middle two rows show the single-band dust temperature predictions from Sommovigo et al. (2022a, S22). We show the inferred dust temperature for two assumed values of the burstiness κ_s in their models; the original value assumed by Sommovigo et al. (2022a) and the updated values based on the measured [O III]/[C II] ratios as discussed in this work ($\kappa_s \sim 15 - 20$). For REBELS-12, we show the predicted temperatures based on the inferred burstiness for the total system, and just the [O III]-bright component. In addition, we show the dust temperature predictions from Fudamoto et al. (2022a, F22) in the bottom row. While a larger sample size is required for a more detailed comparison, the single-band dust temperature models successfully predict the dust temperatures measured from the two-band fit for REBELS-25 and REBELS-38 under careful assumptions on the burstiness parameter and/or infrared sizes.

two dust components seen in the Band 8 data separately (assuming $r_{\text{IR}} = 1.0 \pm 0.3 \text{ kpc}$ for both clumps A&B), but also find that they are characterized by a near-identical dust temperature.

We show the predicted dust temperatures using the Fudamoto et al. (2022a) models in Figure B1 (bottom row). We assume a conserva-

tive systematic 11 K uncertainty – resulting from the assumption of a fixed clumpiness – and add it in quadrature to the fitting uncertainties, following the discussion in Fudamoto et al. (2022a). We find that, despite the aforementioned uncertainties and caveats, the predicted single-band dust temperatures are in good agreement with the values derived from MBB fitting. Interestingly, a relatively large temperature of $T_{\text{dust}} = 61 \pm 13 \text{ K}$ is predicted for REBELS-12, driven predominantly by its large UV luminosity ($L_{\text{UV}} \approx 2 \times 10^{11} L_{\odot}$). Deeper ALMA observations of REBELS-12 at either Band 6 or 8 are required to verify if it indeed hosts warmer dust than REBELS-25 and REBELS-38.

APPENDIX C: MBB FITTING OF LITERATURE SAMPLE

In Section 6.2, we consistently analyze the dust SEDs of thirteen $z \gtrsim 5.5$ literature sources targeted at two or more ALMA bands, at least one of which provides a continuum detection. We list the parameters obtained from modified blackbody fitting in Table C1. We note that for sources with poor photometry (e.g., a single, modest-S/N dust detection and one or multiple upper limits), the inferred dust temperatures – and therefore the inferred dust masses and IR luminosities – depend strongly on the adopted prior on T_{dust} , as discussed in the main text.

Table C1. Dust parameters derived from optically thin modified blackbody fitting to thirteen $z \geq 5.5$ literature sources, using either a fixed dust emissivity index ($\beta = 1.5, 2.0$) or a Gaussian prior on β .

References: B20: Bakx et al. (2020), B21: Bakx et al. (2021), F20: Faisst et al. (2020), H20: Harikane et al. (2020), L17: Laporte et al. (2017), L19: Laporte et al. (2019), M22: Morishita et al. (2022), O22: Ono et al. (2022), Sugahara et al. (2021), W22: Wistok et al. (2022).

	A1689-zD1	A2744-YD4	Big Three Dragons	COS-3018555981	HZ4	HZ6	HZ9
Reference	B21	L17, L19, M22	H19, S21	W22	F20	F20	F20
β	1.5	1.5	1.5	1.5	1.5	1.5	1.5
$\log_{10}(M_{\text{dust}}/M_{\odot})$	$7.13^{+0.14}_{-0.13}$	$5.51^{+0.25}_{-0.20}$	$6.73^{+0.52}_{-0.37}$	$7.39^{+0.67}_{-0.57}$	$6.60^{+0.33}_{-0.20}$	$7.95^{+0.37}_{-0.43}$	$7.54^{+0.16}_{-0.19}$
T_{dust} [K]	45^{+4}_{-4}	143^{+36}_{-43}	88^{+59}_{-37}	37^{+23}_{-11}	122^{+45}_{-45}	36^{+15}_{-8}	61^{+15}_{-9}
$\log_{10}(L_{\text{IR}}/L_{\odot})$	$11.28^{+0.08}_{-0.08}$	$12.39^{+0.41}_{-0.63}$	$12.49^{+0.85}_{-0.77}$	$11.09^{+0.60}_{-0.33}$	$13.14^{+0.55}_{-0.77}$	$11.56^{+0.41}_{-0.22}$	$12.42^{+0.33}_{-0.24}$
β	2.0	2.0	2.0	2.0	2.0	2.0	2.0
$\log_{10}(M_{\text{dust}}/M_{\odot})$	$7.28^{+0.15}_{-0.14}$	$5.48^{+0.29}_{-0.20}$	$6.99^{+0.60}_{-0.54}$	$7.71^{+0.63}_{-0.51}$	$6.72^{+0.43}_{-0.30}$	$8.33^{+0.40}_{-0.39}$	$7.92^{+0.14}_{-0.14}$
T_{dust} [K]	39^{+3}_{-3}	138^{+38}_{-44}	62^{+55}_{-23}	31^{+11}_{-6}	98^{+56}_{-40}	28^{+7}_{-5}	42^{+6}_{-4}
$\log_{10}(L_{\text{IR}}/L_{\odot})$	$11.25^{+0.08}_{-0.08}$	$12.73^{+0.48}_{-0.73}$	$12.17^{+1.12}_{-0.66}$	$11.03^{+0.37}_{-0.22}$	$13.11^{+0.87}_{-0.93}$	$11.42^{+0.25}_{-0.16}$	$12.09^{+0.18}_{-0.15}$
β	$1.7^{+0.5}_{-0.4}$	$2.1^{+0.4}_{-0.4}$	$1.5^{+0.5}_{-0.4}$	$1.5^{+0.5}_{-0.5}$	$1.7^{+0.4}_{-0.4}$	$1.5^{+0.5}_{-0.5}$	$1.4^{+0.5}_{-0.4}$
$\log_{10}(M_{\text{dust}}/M_{\odot})$	$7.19^{+0.20}_{-0.18}$	$5.47^{+0.31}_{-0.23}$	$6.77^{+0.59}_{-0.39}$	$7.42^{+0.75}_{-0.71}$	$6.65^{+0.42}_{-0.24}$	$7.91^{+0.54}_{-0.66}$	$7.46^{+0.45}_{-0.44}$
T_{dust} [K]	42^{+7}_{-6}	136^{+39}_{-46}	84^{+62}_{-38}	36^{+32}_{-11}	111^{+51}_{-47}	37^{+32}_{-11}	66^{+56}_{-24}
$\log_{10}(L_{\text{IR}}/L_{\odot})$	$11.27^{+0.09}_{-0.09}$	$12.75^{+0.62}_{-0.77}$	$12.39^{+0.82}_{-0.74}$	$11.10^{+0.65}_{-0.33}$	$13.06^{+0.70}_{-0.84}$	$11.58^{+0.62}_{-0.25}$	$12.50^{+0.70}_{-0.44}$
	HZ10	J0217-0208	J1211-0118	MACS0416-Y1	UVISTA-Z-001	UVISTA-Z-019	
Reference	F20	H20, O22	H20, O22	B20	W22	W22	
β	1.5	1.5	1.5	1.5	1.5	1.5	
$\log_{10}(M_{\text{dust}}/M_{\odot})$	$8.09^{+0.09}_{-0.10}$	$7.17^{+0.80}_{-0.67}$	$7.11^{+0.69}_{-0.55}$	$5.82^{+0.26}_{-0.17}$	$6.73^{+0.87}_{-0.68}$	$6.50^{+0.70}_{-0.34}$	
T_{dust} [K]	54^{+6}_{-6}	57^{+67}_{-25}	65^{+66}_{-29}	143^{+35}_{-43}	65^{+71}_{-30}	100^{+59}_{-55}	
$\log_{10}(L_{\text{IR}}/L_{\odot})$	$12.66^{+0.15}_{-0.14}$	$11.88^{+1.20}_{-0.61}$	$12.16^{+1.11}_{-0.74}$	$12.72^{+0.39}_{-0.59}$	$11.74^{+1.08}_{-0.69}$	$12.54^{+0.82}_{-1.18}$	
β	2.0	2.0	2.0	2.0	2.0	2.0	
$\log_{10}(M_{\text{dust}}/M_{\odot})$	$8.44^{+0.09}_{-0.09}$	$7.54^{+0.91}_{-0.89}$	$7.49^{+0.73}_{-0.74}$	$5.78^{+0.31}_{-0.20}$	$6.90^{+0.96}_{-0.93}$	$6.49^{+0.72}_{-0.36}$	
T_{dust} [K]	39^{+3}_{-3}	40^{+53}_{-15}	44^{+47}_{-16}	135^{+39}_{-44}	51^{+73}_{-21}	96^{+61}_{-52}	
$\log_{10}(L_{\text{IR}}/L_{\odot})$	$12.41^{+0.10}_{-0.09}$	$11.61^{+1.29}_{-0.42}$	$11.79^{+1.17}_{-0.51}$	$12.98^{+0.48}_{-0.73}$	$11.61^{+1.35}_{-0.57}$	$12.80^{+0.96}_{-1.31}$	
β	$1.8^{+0.5}_{-0.5}$	$1.6^{+0.5}_{-0.5}$	$1.6^{+0.5}_{-0.5}$	$2.1^{+0.4}_{-0.4}$	$1.6^{+0.5}_{-0.5}$	$1.8^{+0.5}_{-0.5}$	
$\log_{10}(M_{\text{dust}}/M_{\odot})$	$8.30^{+0.34}_{-0.41}$	$7.25^{+0.88}_{-0.72}$	$7.18^{+0.78}_{-0.60}$	$5.78^{+0.32}_{-0.22}$	$6.76^{+0.93}_{-0.72}$	$6.49^{+0.72}_{-0.35}$	
T_{dust} [K]	44^{+23}_{-10}	52^{+69}_{-23}	60^{+69}_{-28}	134^{+39}_{-46}	62^{+72}_{-29}	99^{+59}_{-54}	
$\log_{10}(L_{\text{IR}}/L_{\odot})$	$12.49^{+0.38}_{-0.20}$	$11.81^{+1.17}_{-0.56}$	$12.06^{+1.08}_{-0.69}$	$12.97^{+0.62}_{-0.74}$	$11.68^{+1.11}_{-0.63}$	$12.62^{+0.96}_{-1.22}$	